JBC RESEARCH ARTICLE

An acyl-adenylate mimic reveals the structural basis for substrate recognition by the iterative siderophore synthetase DesD

Received for publication, April 12, 2022, and in revised form, June 13, 2022 Published, Papers in Press, June 21, 2022,
https://doi.org/10.1016/j.jbc.2022.102166

Jinping Yang[1,‡], **Victoria S. Banas**[1,‡], **Ketan D. Patel**[2,‡], **Gerry S. M. Rivera**[1], **Lisa S. Mydy**[2], **Andrew M. Gulick**[2,*], **and Timothy A. Wencewicz**[1,*]

From the [1]*Department of Chemistry, Washington University in St Louis, St Louis, Missouri, USA;* [2]*Department of Structural Biology, Jacobs School of Medicine & Biomedical Sciences at the University at Buffalo, Buffalo, New York, USA*

Edited by Chris Whitfield

Siderophores are conditionally essential metabolites used by microbes for environmental iron sequestration. Most *Streptomyces* strains produce hydroxamate-based desferrioxamine (DFO) siderophores composed of repeating units of N^1-hydroxy-cadaverine (or N^1-hydroxy-putrescine) and succinate. The DFO biosynthetic operon, *desABCD*, is highly conserved in *Streptomyces*; however, expression of *desABCD* alone does not account for the vast structural diversity within this natural product class. Here, we report the *in vitro* reconstitution and biochemical characterization of four DesD orthologs from *Streptomyces* strains that produce unique DFO siderophores. Under *in vitro* conditions, all four DesD orthologs displayed similar saturation steady-state kinetics (V_{max} = 0.9–2.5 μM·min^{-1}) and produced the macrocyclic trimer DFOE as the favored product, suggesting a conserved role for DesD in the biosynthesis of DFO siderophores. We further synthesized a structural mimic of N^1-hydroxy-N^1-succinyl-cadaverine (HSC)-acyl-adenylate, the HSC-acyl sulfamoyl adenosine analog (HSC-AMS), and obtained crystal structures of DesD in the ATP-bound, AMP/PP_i-bound, and HSC-AMS/P_i-bound forms. We found HSC-AMS inhibited DesD orthologs (IC_{50} values = 48–53 μM) leading to accumulation of linear trimeric DFOG and *di*-HSC at the expense of macrocyclic DFOE. Addition of exogenous PP_i enhanced DesD inhibition by HSC-AMS, presumably *via* stabilization of the DesD–HSC-AMS complex, similar to the proposed mode of adenylate stabilization where PP_i remains buried in the active site. In conclusion, our data suggest that acyl-AMS derivatives may have utility as chemical probes and bisubstrate inhibitors to reveal valuable mechanistic and structural insight for this unique family of adenylating enzymes.

Desferrioxamines (DFOs) are hydroxamate-backbone siderophores produced by a variety of environmental bacteria and fungi (1). The DFO natural product class is structurally defined by repeating units of N^1-hydroxy-N^1-succinyl-cadaverine (HSC) joined *via* amide linkages. More than 40 compounds in this class have been discovered including dimeric, trimeric, linear, and macrocyclic analogs (Fig. 1) (2, 3). Despite this structural diversity, the DFO biosynthetic gene cluster *desABCD* is highly conserved with >80% pairwise sequence identity in *Streptomyces* (Fig. S1) (1). DFO biosynthesis is achieved using L-Lys as the primary feedstock where decarboxylation (DesA, PLP), N^1-hydroxylation (DesB, FAD, NADPH, O_2), and N^1-succinylation (DesC, succinyl-CoA) generate the monomeric hydroxamate intermediate HSC (Fig. 2) (4, 5). DesD is a type IV ribosome-independent nonthiotemplated siderophore synthetase (6) that catalyzes the iterative and ATP-dependent condensation of HSC *via* the formation of an HSC–acyl-adenylate intermediate (7, 8). In *Streptomyces coelicolor*, two molecules of HSC are condensed to form the dimeric intermediate *di*-HSC followed by another round of condensation with a third HSC monomer to generate trimeric DFOG. Additionally, DesD catalyzes macrolactamization of DFOG to DFOE (7), presumably *via* a DFOG–acyl-adenylate intermediate. The combined activity of DesA–D using L-Lys and succinyl-CoA as feedstocks does not account for the full structural diversity of DFO analogs (9), including the attachment of antibiotic moieties to sideromycins such as ferrimycin (10, 11) and salmycin (12), which presumably requires additional biosynthetic enzymes (Fig. 1).

DesD and related type IV siderophore synthetases have received less attention than canonical type I thiotemplated nonribosomal peptide synthetases (NRPSs) known to produce a wide range of peptide-based siderophores (13). Both DesD-type siderophore synthetases and NRPS adenylation (A) domains catalyze the conversion of ATP and carboxylate substrates to PP_i and the corresponding acyl-adenylate used in downstream construction of amide bonds that form the backbone of peptide-based siderophores that include hydroxamate, catecholate, and other ligand types. Hence, the type IV siderophore synthetases are often referred to as nonribosomal-peptide-synthetase-independent siderophore (NIS) synthetases (14, 15). In most cases, the substrate carboxylates (often citrate, succinate, glutamate, or derivatives thereof) react with hydroxamate-type ligands derived from Lys or Orn. The

‡ These authors contributed equally to this work.
* For correspondence: Andrew M. Gulick, amgulick@buffalo.edu; Timothy A. Wencewicz, wencewicz@wustl.edu.

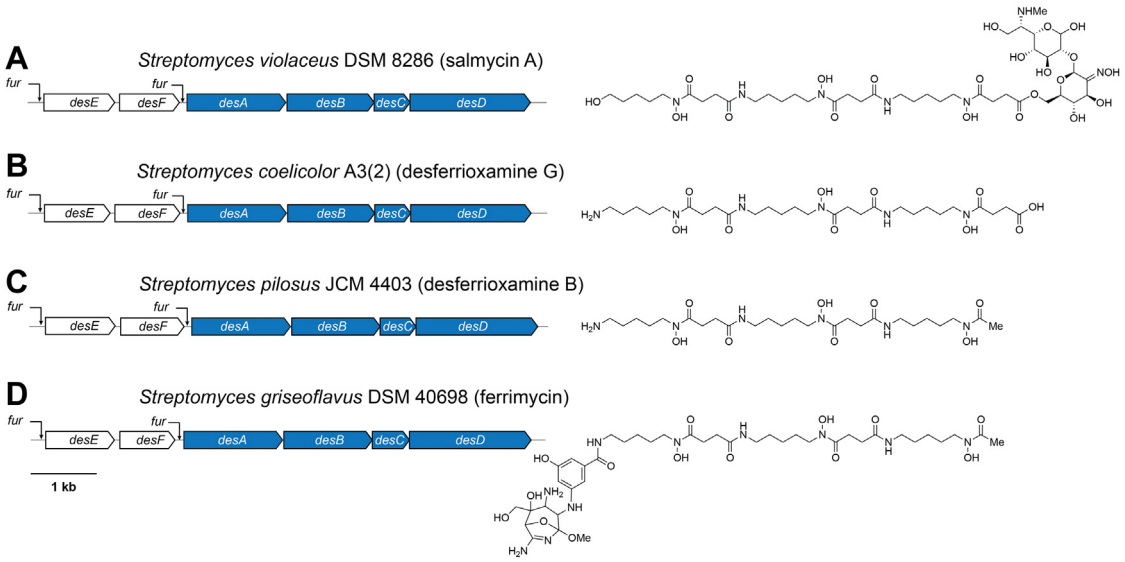

Figure 1. The *desABCD* biosynthetic operon (*blue*) is conserved amongst *Streptomyces* and does not inherently account for structural diversity in the desferrioxamine family of natural products. Genes encoding the siderophore-binding protein (*desE*) and siderophore reductase (*desF*) genes are shown in *white*. *A*, *Streptomyces violaceus* DSM 8286 produces the sideromycin salmycin A. *B*, *Streptomyces coelicolor* A3(2) produces the siderophore desferrioxamine G (DFOG). *C*, *Streptomyces pilosus* JCM 4403 produces the siderophore desferrioxamine B (DFOB). *D*, *Streptomyces griseoflavus* DSM 40698 produces the sideromycin ferrimycin.

hydroxamates are formed *via* tandem *N*-hydroxylation and *N*-acylation of available free amino groups catalyzed by FAD-dependent *N*-monooxygenase and *N*-acyl transferase enzymes, respectively, similar to that described previously for DesB and DesC in DFO biosynthesis. Both NRPS and NIS adenylating enzymes activate carboxylate substrates *via* formation of the corresponding acyl-adenylate with formation of PP_i as byproduct (16, 17). In NIS synthetases, the PP_i remains bound deep in the enzyme active site occluded by the tightly bound acyl-adenylate (18). The acyl-adenylate is directly condensed with an amine nucleophile (or less commonly with a hydroxyl nucleophile) accommodated in the enzyme active site resulting in nonthiotemplated amide bond (ester bond, less common) formation with loss of AMP (18). This two-step

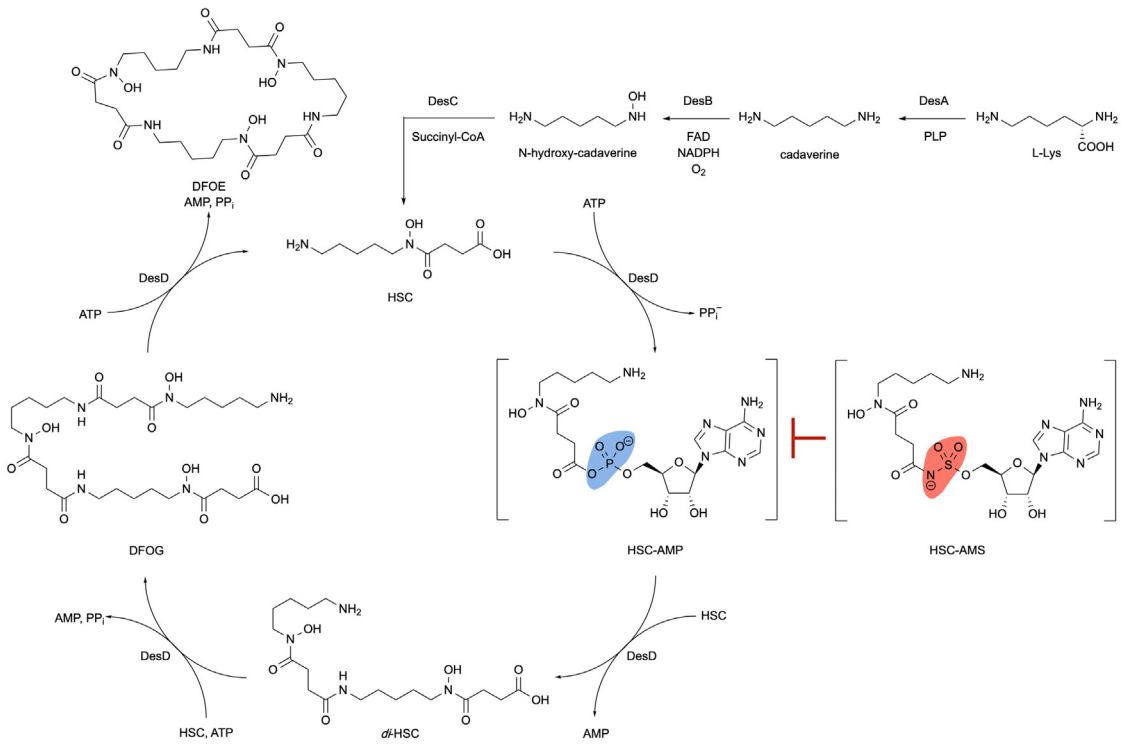

Figure 2. Biosynthetic conversion of L-Lys to HSC by DesABC and proposed catalytic cycle for the iterative conversion of HSC to DFOE by DesD. The HSC-AMS inhibitor synthesized in this work is highlighted to show structural resemblance to the putative HSC-AMP acyl-adenylate intermediate. DFOE, desferrioxamine E; HSC, N^1-hydroxy-N^1-succinyl-cadaverine.

reaction requires coordinated binding and catalysis involving three substrates (ATP, carboxylate, and amine/alcohol).

NIS synthetases have been further classified as type A–C based on the chemical nature of the carboxylate substrate (citrate, α-ketoglutarate, or citrate/succinate derivatives, respectively) and sequence identity (14, 15). Protein structures of representative members of all three types have been determined, with AcsD from achromobactin biosynthesis (19), and IucA from aerobactin biosynthesis (20) representing type A enzymes and SbnC from staphyloferrin B biosynthesis (21) representing type B. Five type C enzymes have been structurally characterized: AlcC (alcaligin) (22), AsbB (petrobactin) (23), IucC (aerobactin) (24), DfoC (DFOE) (25), and DesD (DFOs) (7). The NIS synthetases from all three types adopt a shared fold that has been compared to an open left hand, with thumb, finger, and palm domains stretching from the N to the C terminus. The active site sits in the palm domain with enzymes often showing disordered loops from the finger and palm domain in the absence of ligands. Several enzymes have been crystallized with ATP, illustrating a common binding pocket for the nucleotide. In contrast, only the NIS synthetase involved in achromobactin biosynthesis, AcsD, has been crystallized bound to ligands other than ATP. AcsD condenses citrate with the side chain hydroxyl of serine through a citryl-adenylate intermediate. Incubation of the protein with ATP, citrate, and the substrate analog ethylenediamine resulted in the capture of a cocrystal with Mg·ATP and the product analog (3′*S*)-*N*-citryl-ethylenediamine (26). This structure identified residues that were probed by site-directed mutagenesis, identifying Glu442 and Arg501 that were important for catalytic activity.

Studies of the type A synthetase IucA from aerobactin biosynthesis have been performed to examine the catalytic mechanism (18). IucA catalyzes the stereoselective addition of N^6-acetyl-N^6-hydroxylysine to a primary carboxylate of citrate to form N^2-(3*S*-citryl)-N^6-acetyl-N^6-hydroxylysine (24). The examination of the steady-state terreactant mechanism showed ordered catalysis with ATP binding first, citrate binding second, and the modified lysine nucleophile binding last. Formation of the quaternary complex with all three substrates occurred prior to chemistry, and both partial reactions, the adenylation of citrate and the amide bond formation, occur prior to release of any of the three products. In the case of iterative NIS synthetases such as DesD, presumably there is some degree of volume control for binding a variety of monomeric, dimeric, and trimeric ligands including substrates, intermediates, and products (7). The sequential chemistry of the adenylation and amide-formation steps occur in the same position, with the carboxylate attacking the α-phosphate of ATP to form the corresponding acyl-adenylate/PP_i in the first step and the amine nucleophile attacking the carbonyl of the acyl-adenylate in the second step. This second step results in acyl substitution to displace the AMP leaving group *via* a transient tetrahedral intermediate to form the amide bond, with PP_i release completing enzyme turnover.

The iterative nature of DesD (type C NIS synthetase) presents an additional challenge for gaining a mechanistic understanding of enzyme function in this case. Prior mechanistic studies by Challis (4, 8), Codd (27), Hoffmann (7), and Böttcher (28–30) showed that the available substrate pool and DesD active site environment play a role in determining product outcome (*i.e.*, dimer *versus* trimer or linear *versus* macrocyclic), but the complete mechanism for HSC oligomerization in DFOG/DFOE biosynthesis is not known. We hypothesized that DesD orthologs from *Streptomyces* that produce structurally diverse DFO analogs will display unique active site structures and substrate selectivity resulting in unique product outcomes (Fig. 1). Here, we tested this hypothesis through the structural and biochemical characterization of four DesD orthologs (83%–87% pairwise sequence identity) from *Streptomyces violaceus* (SvDesD; produces salmycin), *S. coelicolor* (ScDesD; produces DFOG and DFOE), *Streptomyces pilosus* (SpDesD; produces DFOB), and *Streptomyces griseoflavus* (SgDesD; produces ferrimycin) (Fig. 1). We found that all the DesD orthologs convert synthetic HSC to macrocyclic DFOE as the preferred thermodynamic product with varying accumulation levels of intermediate *di*-HSC and linear trimeric DFOG. We synthesized an HSC-acyl sulfamoyl adenosine analog (HSC–((*2R,3S,4R,5R*)-5-(6-amino-9H-purin-9-yl)-3,4-dihydroxytetrahydrofuran-2-yl)methyl sulfamate [AMS]) as a bisubstrate mimic of the putative HSC acyl-adenylate intermediate produced in the DesD active site. Inhibition of DesD by HSC-AMS leads to greater accumulation of linear DFOG and *di*-HSC at the expense of macrocyclic DFOE. While acyl AMS analogs are potent (nM) inhibitors of NRPS A-domains (31–34), tRNA synthetases (35–37), and other adenylating enzymes (38–40), we found that HSC-AMS partially inhibits the DesD orthologs with apparent IC_{50} values ∼50 μM. These biochemical studies are complemented by the determination of crystal structures of unliganded SvDesD and unliganded, ATP-bound, AMP/PP_i-bound, and HSC-AMS/P_i-bound SgDesD. The structures show good overall agreement with the previously reported structure of ATP-bound ScDesD (7) and provide additional insight into active site loop dynamics related to substrate binding, acyl-adenylate stabilization, and catalysis. Using the HSC-AMS-bound SgDesD structure as a template, we constructed a molecular docking model for DFOG-AMS that provides new mechanistic insight into dimerization, trimerization, and macrolactamization reactions leading to DFOE formation. These structures and a mechanistic model may serve as a starting point for better understanding NIS synthetase mechanisms and substrate specificity to aid genome mining capabilities for natural products derived from biosynthetic pathways utilizing NIS synthetases.

Results

Selection of DesD orthologs for this study

Five type C NIS synthetases capable of adenylating HSC have been heterologous expressed and biochemically characterized: DesD (DFOs) (7, 8, 27), AlcC (alcalignin) (22), BibC (bisucaberine) (41), AvbD (avaroferrin) (29), and PubC (putrebactin) (30, 42). All these enzymes are capable of

iterative synthetase catalytic activities (HSC adenylation/condensation and macrolactamization). Of these enzymes, only DesD naturally produces *tri*-hydroxamates while AlcC, BibC, AvbD, and PubC all produce macrocyclic *di*-hydroxamate siderophores. Despite the widespread distribution of DesD orthologs in *Streptomyces* and other microbial species (1), the ortholog from *S. coelicolor* (ScDesD) (7, 8) and *Salinospora tropica* (27) remain the only enzymes to be biochemically characterized through *in vitro* reconstitution. It is noteworthy that DfoC from *Erwinia amylovora* is a fusion of DesC and DesD orthologs that has been structurally, but not biochemically, characterized (25). ScDesD produces linear DFOG (minor product) and macrocyclic DFOE (major product) under *in vitro* reaction conditions and can also produce trace quantities of DFOB when provided N^1-hydroxy-N^1-acetyl-cadaverine (HAC) in combination with HSC as substrates (8). *S. pilosus* JCM 4403 (SpDesD) produces DFOB as the major DFO isomer by mass in cell culture (43). DFOB is also the active ingredient in Desferal, an FDA-approved treatment for iron overload diseases (44).

We identified two additional DesD homologs from *S. violaceus* DSM 8286 (SvDesD) and *S. griseoflavus* DSM 40698 (SgDesD) *via* whole genome Illumina sequencing of these strains (GenBank accession numbers: OM145979 and OM145980). *S. violaceus* produces the salmycin family of sideromycin antibiotics that contain a terminal hydroxy-analog of DFOG known as danoxamine joined *via* ester linkage to an unusual oxime-containing amino-disaccharide antibiotic moiety (12). *S. griseoflavus* produces the ferrimycin family of sideromycin antibiotics composed of DFOB joined *via* amide linkage to an amino-hydroxy-benzoic acid functionalized with an apparent aminocyclitol-type antibiotic moiety (10). antiSMASH (45) analysis of the *des* BGCs from *S. coelicolor*, *S. pilosus*, *S. violaceus*, and *S. griseoflavus* revealed high conservation of gene organization and flanking gene identities making these four DesD orthologs a good enzyme set (82.7%–86.8% pairwise amino acid sequence identity) for comparative biochemical and structural characterization (Fig. S1 and Tables S1–S5). We obtained synthetic genes for ScDesD, SpDesD, SvDesD, and SgDesD with codon-optimized sequences for transcription in *Escherichia coli* (Tables S6–S10). All four proteins expressed efficiently with high solubility from an IPTG-inducible pET28a vector in *E. coli* BL21 (DE3) to provide highly pure *N*-His_6-variants after elution from nickel-nitrilotriacetate (Ni-NTA) resin (Fig. S2).

Synthesis of HSC monomeric substrate

The HSC monomer (the product of upstream DesABC enzymes) is the universal building block for DesD in the iterative assembly of DFO-type siderophores (Fig. 2). We envisioned using HSC and ATP as the exclusive substrates for *in vitro* reactions with ScDesD, SpDesD, SvDesD, and SgDesD to best compare steady-state kinetics and product pool compositions across the enzyme set. We adapted the synthetic route developed separately by Miller and Challis to prepare pure HSC for the *in vitro* DesD-catalyzed reactions (Fig. 3) (8, 46). Commercially available 5-amino-1-pentanol (1) was treated with CbzCl under aqueous basic conditions to provide *N*-Cbz-5-amino-1-pentanol (2) in 90% yield after purification. Mitsunobu reaction between compound 2 and *N*-troc-*O*-Bn-hydroxylamine using DEAD and Ph_3P provided N^1-troc-N^1-OBn-N^5-Cbz-cadaverine (3) in 47% yield after purification. Treatment of compound 3 with activated Zn and succinic anhydride in tetrahydrofuran (THF) and acetic acid facilitated a one-pot *trans*-*N*-acylation (troc-to-succinyl) to give N^1-succinyl-N^1-OBn-N^5-Cbz-cadaverine (4) in 84% yield after purification. Final Pd/C-catalyzed hydrogenolysis of compound 4 in MeOH under an atmosphere of H_2 (1 atm) provided HSC in 98% yield with no need for final purification.

In vitro *reconstitution of NIS synthetase activity of four DesD orthologs*

With pure HSC substrate and recombinant ScDesD, SpDesD, SvDesD, and SgDesD in hand, we optimized *in vitro* reaction conditions (buffer composition, enzyme concentration, and substrate concentration) suitable for comparing steady-state kinetics and product formation (Fig. 4*A*). High concentrations of DesD (36.7 μM) and ATP (3 mM) led to high background ATPase activity and rapid formation of macrocyclic DFOE with little *di*-HSC and DFOG detectable by LC-MS analysis of reaction mixtures (Fig. S3). We found that addition of 10% glycerol v/v to the reaction mixture prevented the precipitation of all four DesD orthologs during the course of *in vitro* reactions, consistent with a previous report by the Hoffmann group (7). As opposed to the Hoffmann group findings (frozen protein reportedly maintained activity for ∼9 days), aliquots of our purified DesD constructs maintained activity for >6 months when kept frozen (−80 °C) in dialysis buffer (50 mM K_2HPO_4, 150 mM NaCl, 1 mM DTT, pH 8). Lowering the [DesD] (2 μM) and [ATP] (150 μM) reduced background ATPase activity and allowed for detection of *di*-HSC and DFOG *via* LC-MS to effectively monitor reaction progress along as judged by relative ion counts of accumulating intermediates and products (*di*-HSC, DFOG, and DFOE) (Fig. S4).

Under optimized reaction conditions (31 mM KP_i buffer, 10 mM $MgCl_2$, 150 μM HSC, 150 μM ATP, and 2 μM DesD, 10% v/v glycerol, final working pH of ∼7.2) all four DesD orthologs produced macrocyclic DFOE as the major thermodynamic product (Fig. 4*B*). This supports the notion that additional biosynthetic enzymes, regulatory factors, or substrates are needed to produce diverse DFO structures such as DFOB, salmycin, ferrimycin, and other acylated DFO analogs (Fig. 1). Based on qualitative LC-MS analysis of two time points (5 and 35 min), the four enzymes generated differing amounts of *di*-HSC, DFOG, and DFOE during the reaction (Figs. 4*B* and S4). The accumulation of intermediate *di*-HSC was inconsistent across the four DesD orthologs; however, the accumulation of linear DFOG and macrocyclic DFOE were found to be reproducible. Qualitative analysis of the extracted ion chromatograms (EICs) for DFOG and DFOE after 5 min and 35 min revealed that ScDesD (from the natural producer

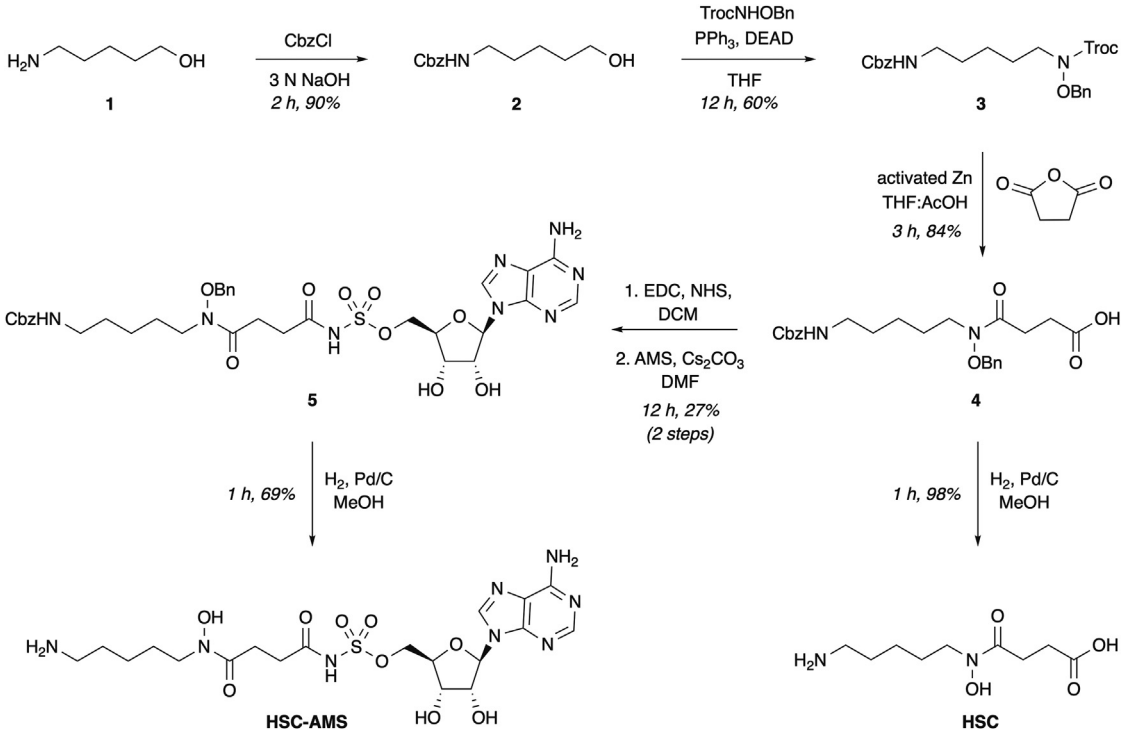

Figure 3. Synthesis of HSC and HSC-AMS. AMS, ((*2R,3S,4R,5R*)-5-(6-amino-9H-purin-9-yl)-3,4-dihydroxytetrahydrofuran-2-yl)methyl sulfamate; HSC, N^1-hydroxy-N^1-succinyl-cadaverine.

of macrocyclic DFOE) generated macrocyclic DFOE at a faster rate than SgDesD, SpDesD, and SvDesD (natural producers of linear DFO analogs) (Fig. S3).

DesD orthologs display similar apparent steady-state kinetics under in vitro *conditions*

We utilized an AMP detection assay (myokinase [MK]/pyruvate kinase/lactate dehydrogenase [LDH] monitoring for NADH oxidation at 340 nm) to measure the apparent steady-state kinetic parameters of ScDesD, SgDesD, SpDesD, and SvDesD with varying concentrations of HSC monomer and saturating concentrations of ATP (Fig. 4*C*) (47). This assay does not distinguish AMP generated during the formation of *di*-HSC, DFOG, or DFOE; thus, we refer only to apparent V_{max} values. We did not attempt to deconvolute the individual apparent K_m and k_{cat} values given the complexity of the reaction mixture (variable concentrations of intermediate substrates and combinations of variable substrate pairs) and the iterative nature of DesD. To minimize the background formation of AMP from uncoupled ATPase activity, control reactions with no substrate were performed (Fig. S5). We found that 200 nM DesD gave no detectable AMP formation above the assay background. Under optimized reaction conditions (31 mM KP_i buffer, 4 U/ml MK, 8.4 U/ml pyruvate kinase, 12.6 U/ml LDH, 1 mM phosphoenolpyruvate, 0.2 mM NADH, 10 mM $MgCl_2$, variable [HSC] (100–2000 μM), 3 mM ATP, and 200 nM DesD, 10% v/v glycerol, final working pH of ∼7.2), all four DesD orthologs displayed similar apparent V_{max} values ranging from 0.9 to 2.5 μM·min^{-1} (95% confidence) and apparent $K_{0.5}$ values ranging from 65 to 350 μM (95% confidence) (Fig. 4*C*). The DesD orthologs were subject to weak substrate/product feedback inhibition. Ortholog SpDesD exhibited the largest decrease in apparent velocity beyond 600 μM HSC, followed by SgDesD, while both ScDesD and SvDesD appear to be less effected by substrate/product inhibition. With the function of all four DesD orthologs validated we set out to explore mechanistic differences using an inhibitor-based approach.

Synthesis of HSC-AMS acyl adenylate mimic

Motivated by the utility of AMS-type inhibitors in studies of diverse adenylating enzymes, we designed an HSC-AMS inhibitor to mimic the putative DesD HSC-AMP acyl-adenylate intermediate (Fig. 2). We leveraged our synthetic route to HSC to prepare the HSC-AMS compound by converting compound 4 into the corresponding *N*-hydroxysuccinimide (NHS) ester *via* treatment with *N*-(3-dimethylaminopropyl)-*N*′-ethylcarbodiimide hydrochloride and NHS in dichloromethane (Fig. 3) (48, 49). The NHS ester was used without further purification in an amide coupling reaction with commercially available AMS in the presence of Cs_2CO_3 and *N*,*N*-dimethylformamide (DMF) solvent to provide fully protected compound 5 in 27% yield (2 steps) after purification. Global deprotection of the *N*-Cbz and *O*-Bn groups provided HSC-AMS in 69% after purification. We found that HSC-AMS was unstable when exposed to strong acid. This prevented the use of an *N*-Boc protecting group (our initial attempt) where the final deprotection resulted in rapid hydrolysis of HSC-AMS to HSC and AMS components. Final purification was carried out using prep-HPLC with

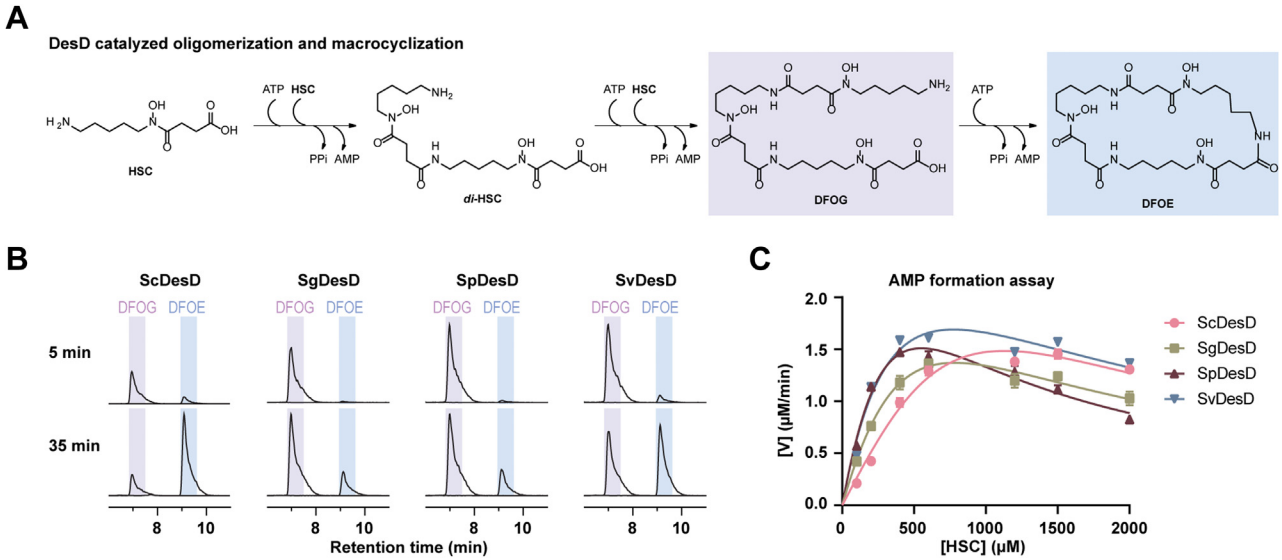

Figure 4. *In vitro* reconstitution of DesD activity reveals similar product profile and steady-state kinetics of four DesD orthologs—ScDesD (*S. coelicolor*), SgDesD (*S. griseoflavus*), SpDesD (*S. pilosus*), SvDesD (*S. violaceus*). *A*, reaction scheme for the *in vitro* DesD reaction resulting in ATP-dependent conversion of synthetic HSC to *di*-HSC, DFOG, and DFOE. *B*, EIC chromatograms for $[M + H]^+$ ions corresponding to DFOG (m/z = 619) and DFOE (m/z = 601) from LC-MS analysis of products from *in vitro* reactions with DesD orthologs taken after quenching aliquots at 5 min and 35 min time points. *C*, steady-state kinetic plots for DesD orthologs under constant ATP and variable HSC conditions. The *x*-axis represents concentration of HSC (μM). The *y*-axis represents velocity as measured by quantified concentrations of DFOG and DFOE collected over three time points. All DesD reactions and LC-MS analyses were performed in duplicate as independent trials. Error bars represent standard deviation. DFOG, desferrioxamine G; EIC, extracted ion chromatogram; HSC, N^1-hydroxy-N^1-succinyl-cadaverine.

ammonium acetate buffer (pH ∼4.75) and acetonitrile (use of TFA or formic acid buffers resulted in hydrolysis of HSC-AMS during purification).

HSC-AMS partially inhibits DesD-catalyzed oligomerization of HSC in vitro

We investigated the ability of HSC-AMS to inhibit DesD-catalyzed oligomerization of HSC using ScDesD and SgDesD (Fig. 5). Apparent DesD inhibition was judged by LC-MS quantification of *di*-HSC, DFOG, and DFOE molecular ions in the presence or absence of HSC-AMS during *in vitro* reactions. To our surprise, we observed only partial inhibition of ScDesD and SgDesD by HSC-AMS at 150 μM under the *in vitro* reaction conditions optimized for steady-state kinetic studies (Fig. 5, *A* and *B*). We observed a reproducible and statistically significant decrease in the relative amount of DFOE formed over a period of 5 h relative to control reactions lacking HSC-AMS or containing only the AMS component (Fig. S4). Formation of DFOE was almost completely inhibited in the case of SgDesD with only trace DFOE detectable by LC-MS at the 5 h time point (Fig. 5*B*). The decrease in DFOE formation correlated with an increase in the accumulation of *di*-HSC and DFOG (Fig. S4). The reason for apparent selective inhibition of DesD at the macrocyclization step (conversion of DFOG to DFOE *via* a presumed DFOG–acyl-adenylate intermediate) by HSC-AMS was unclear.

PP_i improves inhibition of DesD by HSC-AMS

We confirmed *via* LC-MS analysis of the reaction mixture that HSC-AMS was stable during the reaction. We also observed this partial inhibition over a range of conditions including variable enzyme-inhibitor preincubation times and buffer compositions. A breakthrough came when we considered the potential role of PP_i in the inhibition mechanism. Unlike NRPS A-domains and other adenylating enzymes (17), DesD and other NIS-type adenylating enzymes do not release PP_i upon formation of the acyl-adenylate intermediate (20). Hence, we hypothesized that bound PP_i could play a role in stabilizing the HSC-AMS/DesD inhibition complex. To test this hypothesis, SgDesD was equilibrated in the presence of 150 μM HSC-AMS and 150 μM PP_i for 30 min prior to initiation of the reaction by addition of ATP and HSC (both at 150 μM). We observed a significant (>50%) improvement in overall inhibition with PP_i included in the reaction mixture as judged by LC-MS detection of *di*-HSC, DFOG, and DFOE (not detected) (Fig. S4). These optimized conditions allowed us to carefully determine apparent IC_{50} values for HSC-AMS (Fig. S6), which fell in the micromolar range of 38 to 53 μM at 95% confidence with standard error for both ScDesD (43 ± 5 μM; Fig. 5*C*) and SgDesD (50 ± 3 μM; Fig. 5*D*). Other AMS-type bisubstrate inhibitors block the catalytic activity of NRPS A-domains (31–34, 48, 49), tRNA synthetases (50–52), and other adenylating enzymes (53) at concentrations in the nanomolar range. Partial inhibition of DesD at the micromolar concentration range implies that DesD, and possibly other NIS synthetases, stabilize acyl-adenylate intermediates differently than other adenylating enzymes. We hypothesize that this might contribute to the iterative nature of the DesD catalytic mechanism. Hence, we pursued cocrystallization structural studies with HSC-AMS and other ligands/cofactors to better understand substrate recognition, acyl-adenylate stabilization, and mechanism of DesD.

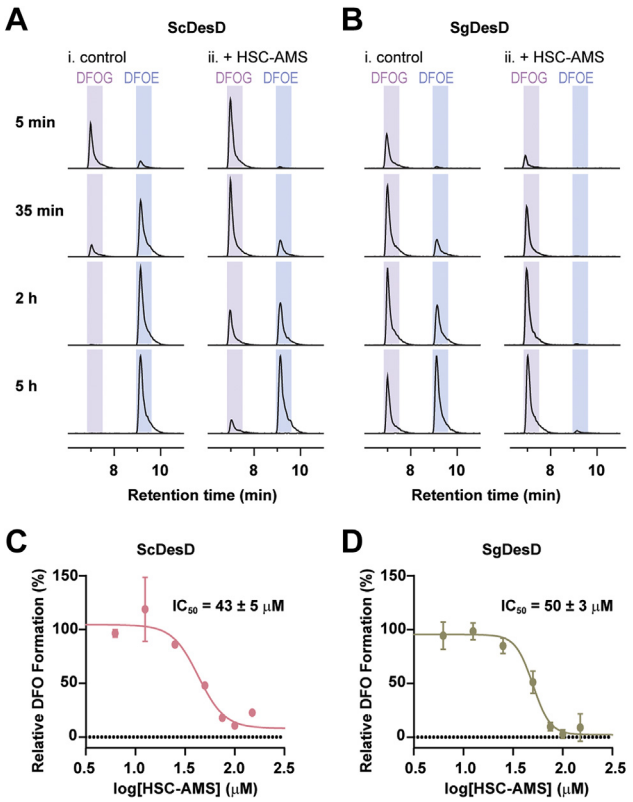

Figure 5. *In vitro* inhibition of DesD activity by HSC-AMS reveals similar potency against two enzyme orthologs. EIC chromatograms for $[M + H]^+$ ions corresponding to DFOG (*m/z* = 619) and DFOE (*m/z* = 601) from LC-MS analysis of products from *in vitro* reactions with (*A*) ScDesD and (*B*) SgDesD in the presence of HSC-AMS (150 μM) and $NaPP_i$ (150 μM) taken after quenching aliquots at 5 min, 35 min, 2 h, and 5 h time points. IC_{50} plots generated from *in vitro* reactions with (*C*) ScDesD and (*D*) SgDesD under steady-state conditions in the presence of constant ATP, constant HSC, and variable HSC-AMS. The *x*-axes represent the log of HSC-AMS concentration (μM). The *y*-axes represent the percentage of combined DFOG and DFOE formed relative to a no inhibitor control (listed as 'Relative DFO Formation (%)'). All DesD reactions and LC-MS analyses were performed in duplicate as independent trials. Error bars represent SD. AMS, ((*2R,3S,4R,5R*)-5-(6-amino-9H-purin-9-yl)-3,4-dihydroxytetrahydrofuran-2-yl)methyl sulfamate; DFO, desferrioxamine; EIC, extracted ion chromatogram; HSC, N^1-hydroxy-N^1-succinyl-cadaverine.

Structures of DesD from S. griseoflavus *and* S. violaceus

To gain structural insights into the function, inhibition, and mechanism of DesD, we solved four structures of SgDesD, an unliganded structure (7TGJ, 2.85 Å) and three complexes with relevant ligands depicting the structure of the enzyme bound to 2 Mg and ATP (7TGK, 2.3 Å); 2 Mg, AMP, and PP_i (7TGL, 2.89 Å); and Mg, HSC-AMS, and P_i (7TGM, 2.5 Å). We also solved the structure of SvDesD in the absence of ligands (7TGN, 2.3 Å).

The structure of unliganded SgDesD was first solved using a single chain of DfoC (25) as the molecular replacement model. SgDesD crystallized with five protomers per asymmetric unit in the $C222_1$ space group (Fig. S7). Gel filtration studies with SgDesD (calculated molecular weight of 68.7 kDa) gave a molecular weight corresponding to 107 kDa, suggesting SgDesD formed a compact dimer in solution (Fig. S8), with an interface that is similar to prior NIS synthetase structures where the thumb and finger domains interact. The structure of SvDesD in the absence of ligands was then solved using SgDesD as a molecular replacement search model in $P4_32_12$ space group with four chains per asymmetric unit. Both structures are similar to each other, as well as to the previously reported structure of ScDesD (7), with RMS of ∼0.6 Å for all Cα positions over the full length of the protein (Fig. S9).

Liganded complexes of both SvDesD and SgDesD were explored *via* cocrystallization and soaking experiments. Two nucleotide-bound complexes of SgDesD were obtained providing views of Mg·ATP (Fig. 6, *A–C*) and Mg·AMP + PP_i (Fig. 6, *D–F*) in the active site. (Electron density for ligands is presented in Fig. S10.) ATP is found to be in the same orientation as in the AMP molecule seen previously in ScDesD (6XRC) (7). The adenosine base of ATP sits between conserved active site residues His153 and His440 in type A and C NIS synthetases. The side chain carboxylate of Glu442 interacts with both α- and γ-phosphates, while the Cβ and Cγ makes hydrophobic interactions with adenosine. A second nucleotide-bound structure illustrated the structure of the protein bound to Mg·AMP and PP_i. Compared to the ATP-bound structures, the α-phosphate of AMP moves away from the PP_i and toward the carboxylate substrate position, matching the orientation of the sulfamoyl group in the HSC-AMS–bound structure described later.

Unlike the ATP-bound structure of ScDesD, which shows a single Mg^{2+} ion (7), the nucleotide complexes of SgDesD show two Mg^{2+} ions that form an elaborate network of interactions with the protein and the triphosphate moieties. One Mg^{2+} ion interacts with an oxygen atom from the α- and γ-phosphates, the bridging oxygen between the α- and β-phosphates, as well as the side chains of Glu442, Asn443, and Asp460. This ion is also observed in the structure of ScDesD bound to ATP. A second Mg^{2+} ion is observed in both the SgDesD·ATP and AMP·PP_i complexes interacting with oxygen atoms from the α- and β-phosphates and the side chains of Asp460, Glu463, and Glu464; a water molecule completes the ion coordination. The α-phosphate oxygens are within hydrogen bonding distance to side chains of Arg303, His440, Glu442, Asn443, and Glu464. The β-phosphate oxygens interact with Arg277, Lys291, Asp460, and Glu463. Finally, the γ-phosphate oxygens are stabilized by a network of interactions with side chains of Ser275, Thr278, Lys291, Arg370, Glu442, Asp460, and Asn443. The same set of residues are found in similar position interacting with ATP phosphates in all types of NIS synthetases, indicating an intricate network of interactions hold the PP_i after the adenylation reaction. All the important residues Ser275, Arg277, Lys291, Arg303, Arg370, His440, Glu442, Asn443, and Asp460 interacting with phosphate oxygens are conserved in all types of NIS synthetases, indicating a conserved pocket for ATP phosphates (Fig. S11).

Structure of HSC-AMS–bound DesD

A variety of synthetic substrates and substrate analogs were used in crystallization trials to obtain insight into the nature of binding of the non-nucleotide substrates. A structure was

obtained for SgDesD cocrystallized with the HSC-AMS that illustrated the binding of the inhibitor and an additional phosphate ion in the PP_i binding pocket (Fig. 6, *G–I*). The acyl-adenylate mimic HSC-AMS showed excellent contiguous density for the entire ligand (Fig. S10) in two chains, while in three chains the density of the terminal amine group was not observed. The adenosine was positioned in a similar position as in other structures, while the sulfonamide mimicked the α-phosphate observed in the AMP·PPi structure. Together, the three nucleotides illustrate the trajectory of the α-phosphate as it goes from ATP to the adenylate intermediate (Fig. S12).

In SgDesD, Met569, and Val570 along with residues Phe156, Met438, Thr496, Leu558, Leu561, and Leu579 from palm and finger domains assemble a hydrophobic groove to accommodate carbon chains of succinyl and pentane portion of HSC substrate (Fig. S13). Asp497 interacts with terminal amine group to anchor the end of substrate. Additionally, Met299 makes close van der Waals interactions with second carbon of succinate. Arg303 of the ATP-binding loop makes a salt bridge with carbonyl oxygen of succinate indicating that, apart from its role in ATP binding, Arg303 may also stabilize the adenylated substrate for condensation reaction. Overall, these interactions may help explain substrate selectivity in NIS-type enzymes. The structure and interaction of the sulfonamide are consistent with an anionic form (Fig. S14). The conformation of the hydroxamate is extended away from the succinate linked AMS group, allowing for an open line of attack by an incoming amine nucleophile.

The HSC-AMS–bound SgDesD structure provides insights into the binding of ATP and the carboxylate substrate and the initial adenylation reaction. All NIS synthetases bind ATP similarly, with conserved interacting residues. However, comparison with AcsD bound to citrate and AMP, the positioning of two carboxylic substrates in the substrate-binding pocket is different. The citrate in AcsD structures (Protein Data Bank [PDB] 2X3J, 2W03) folds over the nucleotide and is positioned nearly parallel to the plane of the adenine ring. In contrast, the larger HSC approaches the α-phosphate from a 90° angle (Fig. S15). Hence, different NIS synthetase types have alternate binding pockets to accommodate their carboxylic substrates for adenylation. Another major difference is observed in the SgDesD Pα3 helix formed from residues Met489 through Thr512 (Fig. S7), which initiates with a 3_{10} helix at 489 through 493. The helix exhibits a pronounced bend at Asp500 that allows the N-terminal half of the helix to bend away from the substrate-binding pocket to provide more room for the cadaverine attachment to succinyl. A similar 3_{10} helix is observed in other known type C NIS enzyme structures AlcC, IucC, DfoC, and ScDesD, and this motif may be a hallmark of type C NIS enzymes to accommodate larger carboxylate substrates.

Comparison of SgDesD with prior structures provides insights into the substrate specificity of NIS synthetase types A, B, and C. We examined several residues that interact with carboxylic substrates for comparison between different characterized enzymes (Fig. 7). Met299 in SgDesD interacts with the carboxylate substrate and its corresponding residue is Leu288 in SbnC. However, a Met or Leu at this position will have a steric clash with citrate in AcsD, where it is replaced with Thr301. In AcsD, Asn302 hydrogen bonds to the citrate and is replaced with glycine residues in SgDesD and SbnC. Lys563 makes a salt bridge with citrate in AcsD, and similarly, Lys552 in SbnC might interact with α-ketoglutarate. However, a lysine at this position in SgDesD may have a steric clash with HSC and is replaced with the shorter residue, Ser556. Met569 and Met438 provide hydrophobic interactions on two sides of HSC in SgDesD, while corresponding residues Arg576 and Glu442 in AcsD make hydrogen bonds with citrate. Asp497 in SgDesD, as noted, makes a hydrogen bond with terminal amine of HSC in SgDesD; the corresponding residues in the other enzymes are expected to be far from the necessary binding pocket for the smaller substrates.

DesD loops and implications for catalysis

Comparing different NIS synthetase structures (Fig. 8), two flexible loops located above the active site adopt different positions or are disordered in some complexes, suggesting that they may play a dynamic role in binding to ligands. The loop formed from residues Leu294-Gly304 (colored *pink* [open] and *yellow* [closed] in Fig. 8, *A* and *C*) interacts primarily with ATP and is labeled the ATP-binding (AB) loop. A second loop from Asn566-Ser576 (colored *green*, Fig. 6, *A* and *B*) is involved in substrate binding and is described as the substrate-binding (SB) loop. In the closed conformation, three residues from the AB loop, Asn298, Met299, and Arg303, interact with ATP (Fig. 6*C*). Asn298 and Met299 interact with the ribose moiety while Arg303 makes hydrogen bonds with the α-phosphate. Asn298 and Met299 are less well conserved in other NIS proteins, while Arg303 is an invariant residue in all NIS synthetases, indicating Arg303 may play a critical role in ATP binding (Fig. 7). Examination of other structurally characterized homologs shows that in IucA (type A) the AB loop adopts a closed conformation with ATP, while in unliganded structure the loop is disordered (20). Similarly, SbnC (type B NIS synthetase) showed closed conformation of AB loop when bound to ATP. Although all structures bound to ATP show a closed AB loop, several proteins, including ScDesD (6NL2), DfoC (5O7O), and AcsD (2W03, 2X3J), also have a closed loop even in the absence of nucleotide.

As noted, the SB loop in SgDesD makes several interactions with the HSC-AMS ligand in the complexed SgDesD structure. Unliganded SgDesD and SvDesD structures along with numerous other NIS synthetase structures have a disordered SB loop. The SB loop helps form a hydrophobic groove with residues Met569 and Val570 to allow binding of HSC during adenylation. SgDesD structures with ATP or AMP/PP_i revealed an ordered SB loop that adopts the same position as that observed when HSC-AMS binds. Therefore, we propose that ATP binding in DesD orients the AB loop, which induces

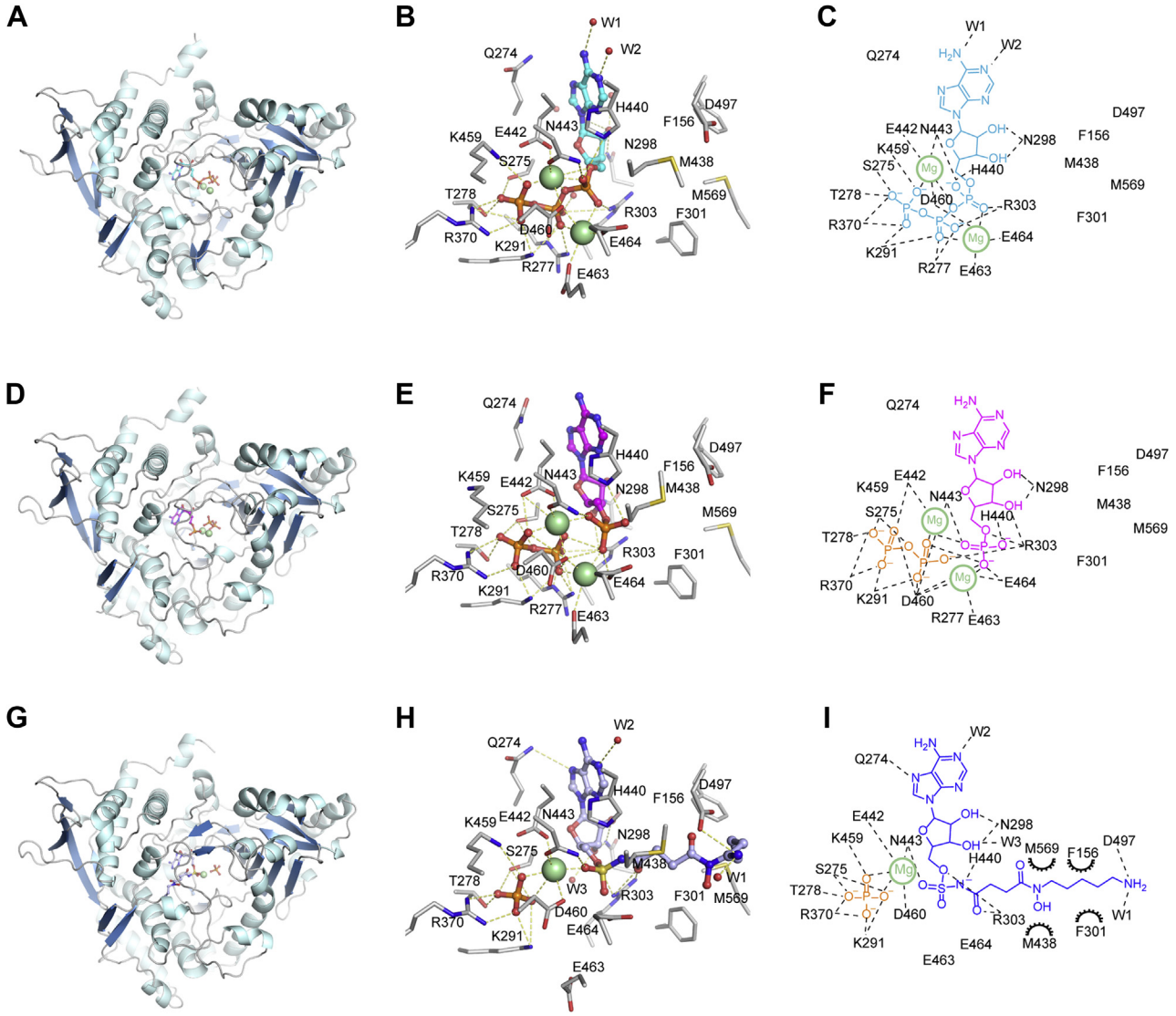

Figure 6. X-ray crystal structures and ligand interaction networks of liganded SgDesD from this work. *A–C*, SgDesD bound to ATP (*cyan*) and 2 Mg; (*D–F*) SgDesD bound to AMP (*magenta*), PP_i and 2 Mg; (*G–I*) SgDesD bound to HSC-AMS (*blue*), P_i, and Mg. AMS, ((*2R,3S,4R,5R*)-5-(6-amino-9H-purin-9-yl)-3,4-dihydroxytetrahydrofuran-2-yl)methyl sulfamate; HSC, N^1-hydroxy-N^1-succinyl-cadaverine.

the SB loop to stabilize and assemble the proper hydrophobic groove that is used to bind the carboxylate substrate, HSC. This interaction of the AB and SB loops are governed by a series of hydrophobic interactions between Met299, Gly300, and Phe301 of the AB loop and Met569 and Val570 of the SB loop. All of these residues contribute to the hydrophobic groove used to bind HSC.

Although the SB loop in other NIS enzymes is shorter and not very well conserved (Figs. S11 and S16), this mechanism is largely consistent across the family of enzymes. The SB loop in the ATP-bound AcsD structure (PDB 2W02) shows movement inward compared to unliganded structure (PDB 3FFE), while citrate-bound structure (PDB 2W03) also orders this loop, particularly, Arg576, toward active site. In the structure of AsbB bound to ATP (PDB 3TO3), the SB loop is ordered. While still interacting with the AB loop, it adopts a different conformation that results in a fairly open active site. Despite the presence of a nucleotide, the SB loop remains disordered in IucA (5JM8) and SbnC (7CBB). Notably, in SbnC, the AB loop appears in a more open conformation that may impact the SB loop orientation. Finally, the SB loop could not be observed in remaining NIS synthetase structures of unliganded IucA, IucC, DfoC, and SbnC, indicating flexibility of the loop in these structures.

Molecular docking of biosynthetic intermediates into DesD

While we were unable to determine the structure of the protein poised for the condensation reaction, we used the experimental structures to perform molecular docking to identify a plausible pose for the condensation reaction. We first tried to dock a monomeric HSC into the structure of SgDesD bound to the HSC-AMS ligand to position an HSC as the attacking nucleophile. Although several models were obtained that directed the primary amine toward the adenylate intermediate, none was particularly convincing, and the flexible

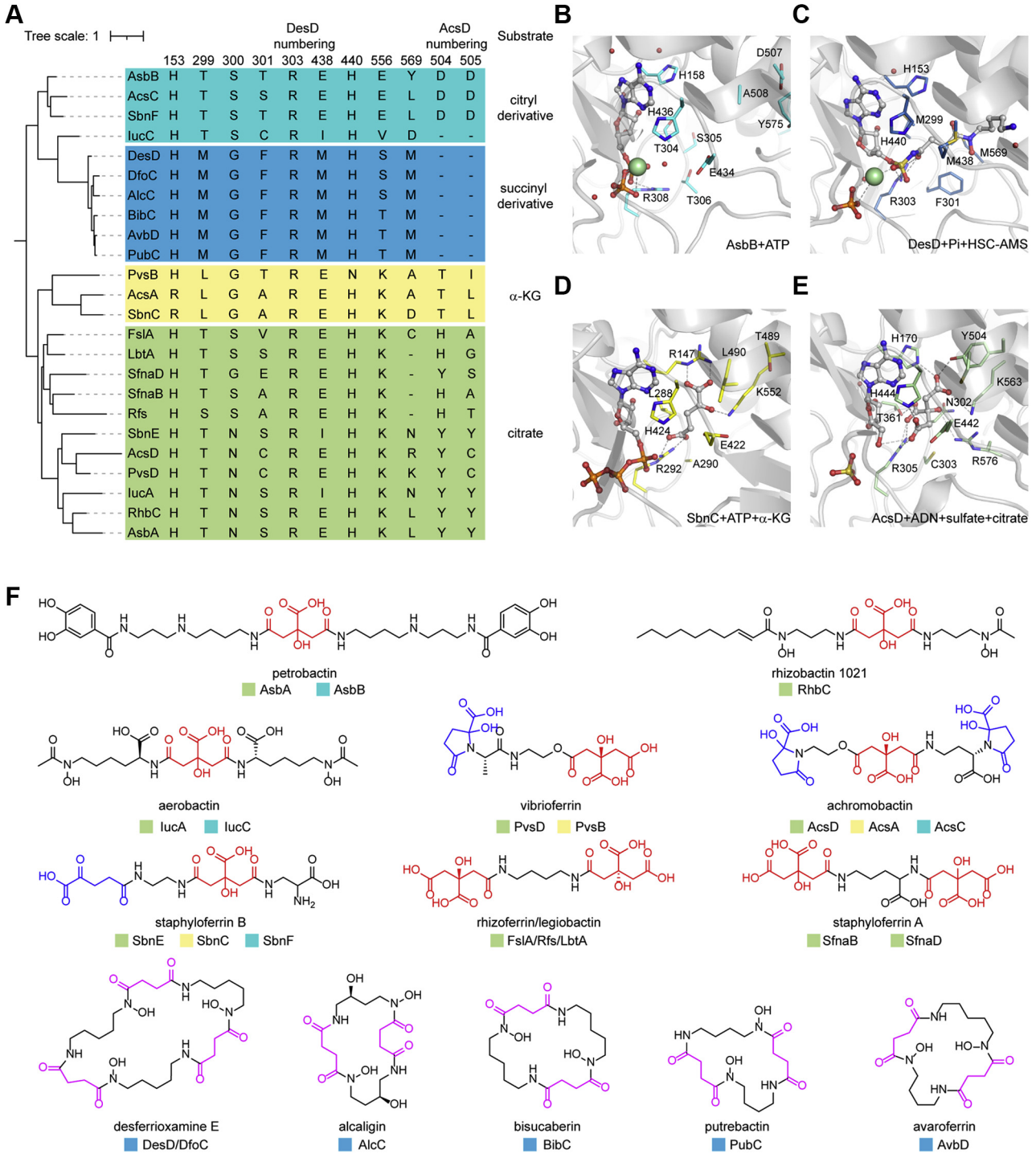

Figure 7. Sequence, structure, and chemical diversity of NIS synthetases. *A*, phylogenetic tree of types A (*green*), B (*yellow*), and C (*teal*/*blue*) NIS enzymes highlighting conserved active site residues involved in substrate recognition. The active site residues are shown in the X-ray crystal structures of (*B*) AsbB bound to ATP and Mg (PDB 3TO3), (*C*) SgDesD bound to HSC-AMS, P_i, and Mg (this work; PDB 7TGM), (*D*) SbnC bound to ATP (PDB 7CBB) with docked α-KG (file available in (21), and (*E*) AcsD bound to adenosine (ADN), sulfate, and Mg (PDB 2W03). Panel (*F*) shows the chemical structures of the siderophore products produced by NIS enzymes from panel (*A*) highlighting citrate, succinate, and α-KG motifs in color. AMS, ((*2R*,*3S*,*4R*,*5R*)-5-(6-amino-9H-purin-9-yl)-3,4-dihydroxytetrahydrofuran-2-yl)methyl sulfamate; HSC, N^1-hydroxy-N^1-succinyl-cadaverine; NIS, nonribosomal-peptide-synthetase-independent siderophore; PDB, Protein Data Bank.

nucleophile appeared to adopt multiple orientations. To assess the docking strategy, we removed the HSC-AMS ligand from the structure and docked the flexible HSC-AMS into a model of the unliganded structure. Here, the top scoring ligand superimposed on the crystallographically observed HSC-AMS for the nucleoside and sulfonamide groups; however, the HSC moiety did not align with the observed structure and instead was directed largely into the open cavity.

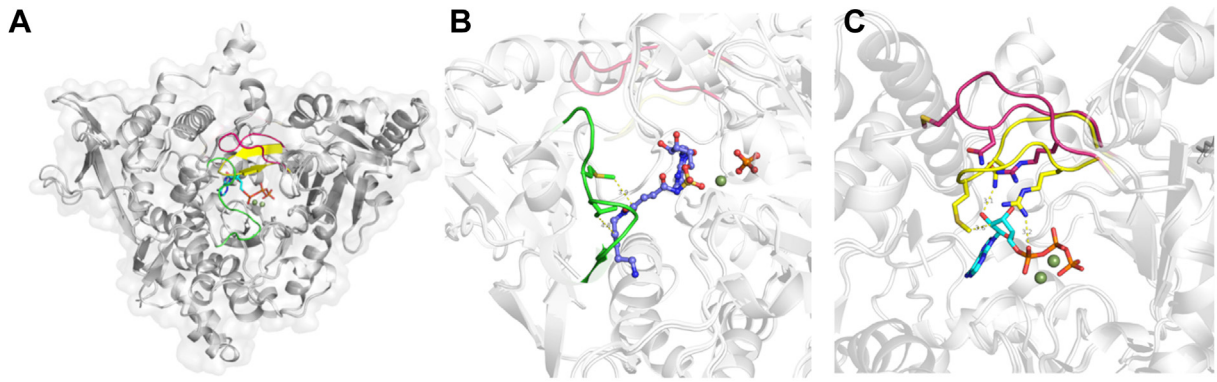

Figure 8. ATP-binding (AB) loop and substrate-binding (SB) loop movements in SgDesD. *A*, positions of AB and SB loops in superposed SgDesD unliganded and ATP-bound structures. AB loop is colored *red* to *yellow* in unliganded and ATP-bound structures, respectively, showing open and closed conformations. SB loop is colored *green* observed only in ATP-bound structure. *B*, SB loop observed only in substrate bound structure shows interaction of Met569 and Val570 with HSC in HSC-AMS–bound SgDesD structure. *C*, AB loop movement from open conformation in unliganded SgDesD (*red*) to closed conformation in ATP-bound SgDesD (*yellow*). Asn298, Met299, and Arg303 show interaction with ATP only in ATP-bound SgDesD structure. AMS, ((*2R*,*3S*,*4R*,*5R*)-5-(6-amino-9H-purin-9-yl)-3,4-dihydroxytetrahydrofuran-2-yl)methyl sulfamate; HSC, N^1-hydroxy-N^1-succinyl-cadaverine.

The precise positioning of the nucleotide moiety gave us the confidence to dock the AMS analog of the linear trimer, DFOG-AMS. This designer DFOG-AMS ligand represents the adenylate intermediate of the final macrocyclization step in DFOE biosynthesis. An extended model of the trimer was manually created and used for the docking reaction. The top scoring model superimposed well over the experimentally observed model for the HSC-AMS and showed an extended substrate that folded back to position the amine, identifying a plausible binding pose for the attacking amine in the condensation site (Fig. 9). In this model, the terminal amine is positioned 5.5 Å from the carbonyl carbon of the adenylate and angled for nucleophilic attack. Interestingly, in the structure of SgDesD bound to HSC-AMS, a glycerol molecule is situated in this nucleophile position, with hydroxyl groups directed toward the carbonyl in several chains.

Discussion

The structure of SgDesD bound to multiple nucleotide ligands furthers our understanding of the nature of the iterative catalytic cycle. The reaction trajectory depicted by the structures confirms the retention of the PP_i product in an internal cavity. The comparison of the structure of SgDesD with AcsD illustrates that while the carboxylate approaches the α-phosphate from the same overall side opposite the PP_i leaving group, the orientation of citrate and HSC are different, and the NIS synthetases probably use variable binding pockets to position the carboxylate for nucleophilic attack on the α-phosphate of ATP. This is to be expected given the diversity of carboxylate substrates that serve as substrates for this broad family of adenylating enzymes.

Beyond comparisons with family members that have different carboxylate substrates, the experimental structures and molecular docking of the linear trimeric HSC-AMS analog reinforce our view that the pocket of DesD is further optimized for binding multiple substrates and pathway intermediates (monomers, dimers, and trimers of HSC) in the biosynthetic cycle. The release of dimeric (*di*-HSC) and trimeric (DFOG) intermediates detected *via* LC-MS suggests reversible binding of substrates, intermediates, and products in the DesD active site. This high degree of substrate plasticity is likely important to allow for iterative turnovers and contributes to the accommodation of mixed substrates and intermediates in the catalytic cycle (not limited to various combinations of HSC); such a scenario is necessary to account for the assembly of DFOB, salmycin, and ferrimycin (Fig. 1). The liganded structure of DesD bound to HSC-AMS provides a rigorous structural model for the adenylation step poised for the condensation reaction. Molecular docking with AMS-type ligands derived from the individual pieces, such as the HSC-AMS inhibitor results in precise positioning of the nucleotide with variable positioning of the HSC groups. This suggests that the active site has the capacity to bind different molecules depending on the stage in the iterative biosynthetic pathway. We propose that there may not be a single "nucleophile-binding site" that can be captured crystallographically or that appears as the lowest energy docking pose. This may explain difficulties by us and others (with multiple NIS synthetases) to capture ligand-bound states beyond the more tightly bound nucleotide. Rather, the large cavity of DesD can accommodate binding to the carboxylate of any of the synthetic intermediates (monomers, dimers, and trimers) for the adenylate forming reaction.

Mechanistic studies with IucA, the NIS synthetase from aerobactin biosynthesis, showed that all three substrates must bind prior to chemistry (18). We propose that this happens for the DesD catalyzed reactions as well as during the extension steps of the cycle. The active site is large enough to enable two free HSC molecules to bind during the dimer forming step. For trimer formation, a HSC dimer and monomer must bind, while for the cyclization reaction, the HSC trimer nearly fills the pocket (Fig. 9), directing the terminal amine back toward the adenylate for the nucleophilic attack and preventing a fourth HSC monomer from entering the pocket.

The directionality of trimer formation is not entirely clear since either monomeric HSC or dimeric *di*-HSC could form the acyl-adenylate or act as the nucleophile to generate the

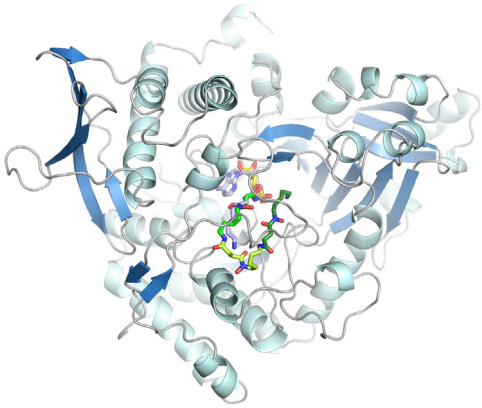

Figure 9. Molecular docking of DFOG-AMS in SgDesD reveals a putative premacrolactamization acyl-adenylate conformation. Each HSC subunit in the trimeric DFOG-AMS structure is highlighted using different shades of *green*. AMS, ((*2R,3S,4R,5R*)-5-(6-amino-9H-purin-9-yl)-3,4-dihydroxytetrahydrofuran-2-yl)methyl sulfamate; DFOG, desferrioxamine G; HSC, N^1-hydroxy-N^1-succinyl-cadaverine.

same trimeric product DFOG followed by macrocyclic DFOE. Directionality becomes important in structures like DFOB, where two molecules of HSC combine with one molecule of HAC to form an HSC-HSC-HAC compound known as DFOB (major product from *S. pilosus*; Fig. 1). Since HAC has no carboxyl group, it can only serve as the nucleophile. This suggests that the formation of DFOB depends on the formation of either homodimeric *di*-HSC or heterodimeric HSC-HAC followed by condensation with either HAC (*via di*-HSC adenylate) or HSC (*via* HSC adenylate), respectively. Given that *di*-HSC appears as a component of nearly all DFO siderophores, this could be a universal biosynthetic intermediate. The relative concentrations of the HSC and HAC likely play a role in partitioning the relative concentrations of dimeric intermediates where DesD is a victim of fate to the composition of the overall substrate pool (monomers, dimers, and trimers). Studies by Challis (4, 8) and more recently by Böttcher (28–30) and Codd (27) support this model and show that the DFO product pool including *N*-acylated derivatives is influenced by the substrate pool composition. There is also correlative evidence for a second cluster of genes in DFO structure diversification, including the amidase encoded by *desG* that commonly correlates with appearance of the *desABCD* operon in microbes (1). Further kinetic, mechanistic, and regulatory studies of DesD and related NIS enzymes in are needed to clarify the model for iterative siderophore assembly in microbes.

AMS ligands have been used in several adenylating enzymes as bisubstrate inhibitors and probes in structural studies where they mimic the acyl-adenylate intermediate (53). In particular, the AMS inhibitors have been very useful for studies of the adenylating enzymes of the NRPS systems, where they have been observed to have apparent K_i values in the low nanomolar range (48). Similarly, other adenylate forming enzymes for which AMS-based analogs are potent inhibitors include the BioA biotin protein ligase (39) with a reported apparent K_D of 0.5 nM and the pantothenate synthetase PanC for which the AMS analog shows an apparent K_i of 220 nM (38). All of these proteins share a common structural feature that allows the AMS inhibitors to inhibit with high affinity. In each case, the carboxylate substrate binds in the core of the protein. The direct inline attack of the carboxylate on the α-phosphate therefore requires the β- and γ-phosphates to project toward the exterior of the protein. In NRPS adenylation domains, a flexible Gly-, Ser-, and Thr-rich loop cradles the β- and γ-phosphates.

In contrast to the structures of NRPS adenylation domain bound to AMS inhibitors, the AMS-bound structure of DesD illustrates how the β- and γ-phosphates project into the core of the enzyme (Fig. S17). As noted previously (20, 54), this structural feature prevents PP_i exchange as a means of assaying the NIS synthetase activity, in contrast to the NRPS adenylation domains (16, 55). More significant, this feature results in the lower potency of the AMS inhibitors for DesD, with apparent K_i values determined to be ∼50 μM. The extensive interactions of the protein with the β- and γ-phosphates impact the binding affinity. Indeed, we found that inclusion of PP_i in the inhibition studies improved the ability of HSC-AMS to inhibit DesD. The pose of ATP in the binding pocket of other adenylating enzymes may therefore be a key consideration in the design of AMS inhibitors for other adenylate-forming enzyme families.

Conclusions

Biochemical characterization of four DesD orthologs (SvDesD, ScDesD, SpDesD, and SgDesD) revealed that macrocyclic DFOE is the thermodynamic product under *in vitro* reaction conditions where HSC is provided as the only substrate building block. Structural characterization of an HSC-AMS bisubstrate inhibitor complexed to SgDesD supported its biochemical characterization as the first reported AMS-type inhibitor of an NIS enzyme family member. Our structural studies revealed that AMS-type inhibitors can identify active site residues and coordinated loop movements important to substrate recognition and catalysis. Molecular docking of a trimeric DFOG-AMS ligand provides insight into the nature of iterative catalysis that enables DesD to produce a wide variety of homodimeric and heterodimeric and trimeric DFO siderophores including linear and macrocyclic analogs. Our findings will inform genome mining efforts for siderophores derived from NIS synthetases and help in refining models for natural product structure prediction.

Experimental procedures

Materials, methods, and instrumentation

All solvents, chemicals, and reagents were purchased from Millipore Sigma, unless otherwise stated. AMS was purchased from Synnovator, Inc. Samples for LC-MS were prepared in 0.45 μM polytetrafluoroethylene mini-UniPrep vials from Agilent. All prep-HPLC was performed using an Agilent/HP 1050 quaternary pump module with an Agilent/HP 1050 MWD module with a Phenomenex Luna 10u C18(2) 100A column, 250 × 21.20 mm, 10 μm with guard column. All LC-MS was performed on an Agilent 6130 quadrupole LC-MS

with G1313 autosampler or G1367B autosampler, G1315 diode array detector, and 1200 series solvent module. A Phenomenex Gemini C18 column, 50 × 2 mm, 5 μm with guard column was used for all LC-MS separations. Mobile phases for prep-HPLC and LC-MS were 0.1% formic acid in (A) H_2O and (B) CH_3CN, and data were processed using ChemStation software (Agilent). NMR was performed on a Varian Unity Inova-500 MHz instrument. The maximum likelihood phylogenetic trees of selected NIS synthetases were built by the "one-click" method from NGPhylogeny.fr (56) and visualized using iTOL v6 (57). Sequence alignments of NIS synthetases were performed by the Clustal Omega online tool from EMBL (58). The alignment results were viewed in ESPript 3.0 (59) and the secondary structure was denoted based on HSC-AMS–bound SgDesD structure (PDB: 7TGM).

Synthetic protocols

The identities of previously reported compounds were confirmed by ^{1}H-NMR and electrospray ionization (ESI) LC-MS analysis. All new synthetic compounds were fully characterized by ^{1}H-NMR, ^{13}C-NMR, gradient COSY, heteronuclear single quantum coherence, and heteronuclear multiple-bond correlation spectroscopy.

Compound 2

Carbamate 2 was prepared as previously reported (13, 46). Briefly, 1-amino-5-pentanol (1) (10 g, 97 mmol) was dissolved in 3 N NaOH (30 ml) in a 100 ml rb flask. CbzCl (11.5 ml, 81 mmol) was added, and the reaction was allowed to stir for 2 h. The reaction was extracted with EtOAc (3 × 200 ml) and then sequentially washed with 1 M HCl (2 × 200 ml), H_2O (2 × 200 ml), and brine (2 × 200 ml). The EtOAc was dried over Na_2SO_4, filtered, and concentrated *via* rotary evaporation under reduced pressure to yield 2 as a clear, colorless oil in 90% yield (17.3 g, 73 mmol). See Figs. S18 and S19 for characterization data and purity analysis (>90% by LC-MS).

Compound 3

2,2,2-trichloroethyl (benzyloxy)carbamate (TrocNHOBn) was prepared using previously reported conditions (46). Briefly, to a solution of *O*-benzylhydroxylamine (20 g, 125 mmol) in H_2O (100 ml) and THF (100 ml), 2,2,2-trichloroethyl chloroformate (TrocCl) (17.2 ml, 125 mmol) was added. Et_3N (17.6 ml, 125 mmol) was added dropwise with stirring. After 3 h at room temperature (RT), the THF was removed *via* rotary evaporation under reduced pressure. The resulting slurry was extracted with EtOAc (2 × 200 ml) and washed with 1 M HCl (2 × 200 ml), H_2O (2 × 200 ml), and brine (2 × 200 ml). The EtOAc was dried over Na_2SO_4, filtered, and concentrated *via* rotatory evaporation under reduced pressure to give TrocNHOBn in 81% yield (30.1 g, 104 mmol). Ph_3P (2.64 g, 10 mmol) and DEAD, 40% in toluene (1.83 ml, 4 mmol) were dissolved in 15 ml of THF in a 100 ml rb flask. Compound 2 (1.2 g, 5.0 mmol) and then TrocNHOBn (3.0 g, 10 mmol) were added sequentially, and the reaction mixture was stirred for 12 h at RT. The THF was removed *via* rotary evaporation under reduced pressure. The resulting residue was dissolved in EtOAc (100 ml) and was washed sequentially with 5% aqueous citric acid (2 × 200 ml), brine (2 × 200 ml), saturated aqueous $NaHCO_3$ (2 × 200 ml), and brine (2 × 200 ml). The EtOAc was dried over Na_2SO_4, filtered, and removed *via* rotatory evaporation under reduced pressure. A mixture of Et_2O and Hex was added to the flask and the solution was filtered through a short path plug of silica gel. The solvent was removed *via* rotary evaporation under reduced pressure and the resulting crude oil was purified by normal phase silica gel column chromatography with a gradient of 100% Hex to 20% EtOAc in Hex. All fractions containing the product as judged by TLC analysis were combined and concentrated *via* rotary evaporation under reduced pressure to provide compound 3 in 60% yield as a pale yellow oil (1.25 g, 2.4 mmol). ^{1}H NMR (500 MHz, CD_3OD) δ (ppm) 7.47 to 7.41 (m, 2H), 7.35 (ddd, J = 13.1, 6.8, 3.5 Hz, 6H), 7.28 (ddt, J = 8.7, 5.9, 3.5 Hz, 2H), 5.05 (s, 2H), 4.92 (s, J = 3.1 Hz, 2H), 4.85 (d, J = 2.0 Hz, 2H), 3.53 (t, J = 7.1 Hz, 2H), 3.09 (t, 2H), 1.64 (m, J = 7.3 Hz, 2H), 1.49 (m, J = 7.1 Hz, 2H), and 1.32 (m, J = 11.0, 9.7, 4.8 Hz, 2H). ^{13}C NMR (126 MHz, CD_3OD) δ (ppm) 158.9, 156.5, 138.5, 136.6, 130.7, 130.7, 129.8, 129.8, 129.5, 129.5, 129.4, 128.9, 128.7, 96.8, 77.9, 76.1, 67.28, 50.4, 41.6, 30.4, 27.7, and 24.8. See Figs. S20–S25 for characterization data and purity analysis (>95% by LC-MS).

Compound 4

Previously reported methods were adapted to prepare compound 4 (13, 46). Compound 3 (324 mg, 0.63 mmol) was dissolved in a mixture of THF (10 ml) and glacial CH_3COOH (10 ml) in a 100 ml rb flask. Activated zinc (324 mg) was added, and the suspension was stirred for 5 min at RT. Succinic anhydride (630 mg, 6.3 mmol) was added slowly as a solid and the reaction mixture was stirred for 3 h under a dry Ar atmosphere. The mixture was filtered through a pad of Celite and concentrated by rotary evaporation under reduced pressure. The resulting residue was dissolved in EtOAc (60 ml) and was washed with brine (2 × 100 ml). The EtOAc was dried over Na_2SO_4, filtered, and removed by rotary evaporation under reduced pressure. The crude solid was dissolved in MeOH and purified *via* RP-C18 prep-HPLC (0% B to 95% B over 17 min, then 95% B to 100% B over 8 min) to give compound 4 as a white solid in 84% yield (232 mg, 0.53 mmol). ^{1}H-NMR and ESI LC-MS were consistent with previous reports of compound 4 (13). See Figs. S26 and S27 for characterization data and purity analysis (>95% by LC-MS).

Compound 5

Preparation of compound 5 was adapted from a previously reported procedure by Aldrich *et al.* (49). *N*-(3-dimethylamino propyl)-*N'*-ethylcarbodiimide hydrochloride–HCl (165.5 mg. 0.863 mmol) was added as a solid to a solution of compound 4 (75 mg, 0.17 mmol) and NHS (64.5 mg, 0.56 mmol) in CH_2Cl_2 (10 ml). The reaction was stirred at RT for 1 h (complete as

judged by TLC analysis). The reaction mixture was diluted with an additional 40 ml of CH_2Cl_2 and washed with 5% aqueous citric acid (100 ml), brine (100 ml), saturated aqueous $NaHCO_3$ (100 ml), and brine (100 ml). The CH_2Cl_2 was dried over anhydrous Na_2SO_4, filtered, and concentrated *via* rotatory evaporation under reduced pressure to give the NHS ester derivative of compound 4 as a clear, colorless oil (61.6 mg, 0.114 mmol). ^{1}H NMR (500 MHz, CD_3Cl) δ (ppm) 7.43 to 7.32 (m, 10H), 5.07 (s, 2H), 4.81 (s, 2H), 3.15 (q, *J* = 6.6 Hz, 2H), 2.90 (q, *J* = 6.9 Hz, 2H), 2.81 to 2.76 (m, 8H), 1.63 (m, *J* = 7.2 Hz, 2H), 1.49 (m, *J* = 7.1 Hz, 2H), and 1.29 (td, *J* = 8.3, 7.7, 4.1 Hz, 2H). See Figs. S28 and S29 for characterization data and purity analysis (>95% by LC-MS).

The NHS ester of compound 4 was used without purification in the preparation of compound 5 using a procedure adapted from the method previously reported by Aldrich *et al.* (49). A solution of the NHS derivative of compound 4 (61.6 mg, 0.114 mmol) and AMS (47.4 mg, 0.137 mmol) was prepared in 6 ml of anhydrous DMF. The solution was treated with $CsCO_3$ (148.3 mg, 0.456 mmol) added as a solid. The reaction mixture was stirred for 12 h at RT under an atmosphere of dry Ar. The DMF was removed by rotary evaporation under high vacuum. The resulting residue was dissolved in MeOH (∼10 mg/ml) and filtered *via* syringe (0.45 μ). The sample was immediately purified by RP-C18 prep-HPLC (0% B to 95% B over 17 min, then 95% B to 100% B over 8 min) to give a light-yellow solid in a 27% yield over two steps (34.6 mg, 0.45 mmol). ^{1}H NMR (500 MHz, CD_3OD) δ (ppm) 8.35 (s, 1H), 8.20 (s, 1H), 7.43 to 7.40 (m, 2H), 7.40 to 7.21 (m, 8H), 6.07 (d, J = 5.0 Hz, 1H), 5.05 (s, 2H), 4.91 (s, 2H), 4.61 to 4.56 (m, 2H), 4.51 (d, J = 3.7 Hz, 1H), 4.40 to 4.28 (m, 1H), 3.65 (d, J = 7.3 Hz, 1H), 3.61 to 3.53 (m, 1H), 3.16 to 3.03 (m, 4H), 2.77 to 2.66 (m, 2H), 2.60 to 2.50 (m, 2H), 1.62 (m, 2H), 1.49 (m, 2H), and 1.45 to 1.39 (m, 2H). ^{13}C NMR (126 MHz, CD_3OD) δ (ppm) 174.2, 166.1, 131.9, 130.9, 130.7, 130.6, 130.0, 129.5, 129.2, 68.5, 66.5, 62.8, 42.8, 38.2, 34.3, 32.9, 32.0, 31.9, 31.6, 26.0, 25.0, 22.1, and 15.7. See Figs. S30–S34 for characterization data and purity analysis (>90% by LC-MS).

HSC-AMS

Compound 5 (21.2 mg, 0.029 mmol) was dissolved in 1 ml MeOH under an Ar atmosphere. The flask was charged with 10% Pd/C (10 mg) and purged with a balloon of H_2. The suspension was stirred under an H_2 atmosphere (1 atm) at RT for 1 h (judged to be complete by LC-MS analysis). The reaction flask was purged with Ar, and the mixture was filtered through a 0.45 μ syringe filter. The MeOH filtrate was concentrated under reduced pressure using rotary evaporation. The resulting crude mixture was purified by RP-C18 prep-HPLC (0% B to 95% B over 17 min, then 95% B to 100% B over 8 min) to afford HSC-AMS in 69% yield (10.3 mg, 0.019 mmol). ^{1}H NMR (500 MHz, DMSO-d_6) δ (ppm) 8.40 (s, 1H), 8.14 (s, 1H), 5.90 (d, J = 6.0 Hz, 1H), 4.61 to 4.57 (m, 1H), 4.27 (dd, J = 6.0, 2.3 Hz, 1H), 4.16 (dd, J = 6.0, 3.0 Hz, 1H), 4.07 to 4.03 (m, 1H), 4.00 (d, J = 6.0 Hz, 1H), 3.51 (t, J = 6.4 Hz, 2H), 2.68 (t, J = 7.0 Hz, 2H), 2.55 to 2.51 (m, 4H), 1.55 to 1.49 (m, 2H), 1.48 to 1.41 (m, 2H), and 1.29 to 1.24 (m, 2H). ^{13}C NMR (126 MHz, DMSO-d_6) δ (ppm) 172.5, 167.7, 159.0, 155.6, 147.6, 134.2, 128.8, 93.0, 86.1, 76.8, 71.3, 61.4, 54.8, 40.6, 32.5, 28.3 26.9, 26.0, and 23.4. See Figs. S35–S39 for characterization data and purity analysis (>90% by LC-MS).

HSC

Compound 4 (116 mg, 0.263 mmol) was dissolved in 2 ml MeOH under an Ar atmosphere. The flask was charged with 10% Pd/C (20 mg) and purged with a balloon of H_2. The suspension was stirred under an H_2 atmosphere (1 atm) at RT for 1 h (judged to be complete by LC-MS analysis). The reaction flask was purged with Ar, and the mixture was filtered through a 0.45 μ syringe filter. The MeOH filtrate was concentrated under reduced pressure using rotary evaporation to give HSC as a white solid in 98% yield (56.4 mg, 0.26 mmol). The compounds were used without purification. ^{1}H NMR and ESI LC-MS were consistent with previous reports of synthetic HSC (8). ^{1}H NMR (500 MHz, CD_3OD) δ (ppm) 3.59 to 3.73 (m, 2 H), 2.79 to 2.92 (m, 2 H), 2.63 to 2.72 (m, 3 H), 2.50 to 2.58 (m, 2 H), 1.66 (dd, *J* = 13.7, 6.8 Hz, 2 H), 1.58 to 1.64 (m, 2 H), and 1.39 ppm (dq, *J* = 15.0, 7.7 Hz, 2 H). See Figs. S40 and S41 for characterization data and purity analysis (>95% by LC-MS).

Expression and purification of DesD proteins for in vitro reconstitution

The pET28-a(+) plasmids containing *desD* genes were purchased from Genscript and transformed into *E. coli* BL21 (DE3) for the purpose of heterologous protein (SgDesD, SvDesD, ScDesD, and SpDesD) expression. Cells harboring protein expression plasmids were grown in 1 l terrific broth (TB) (12 g/l tryptone, 24 g/l yeast extract, 5 g/l glycerol, 17 mM KH_2PO_4, 72 mM K_2HPO_4) with 50 μM kanamycin at 37 °C in a 2.8 l baffled flask. Once the absorbance (A_{600}) reached ∼0.4, the cell culture was cold-shocked on an ice bath to ∼15 °C and induced by adding 0.5 mM IPTG (final concentration). Induced cells were grown at 18 °C with agitation for 18 h, isolated *via* centrifugation (5000 rpm, 20 min, 4 °C), and resuspended in 40 ml of lysis buffer (50 mM K_2HPO_4, 500 mM NaCl, 5 mM β-mercaptoethanol, 20 mM imidazole, 10% glycerol, pH 8). Cell suspensions were flash-frozen in liquid nitrogen, thawed, and lysed by passing through an Emulsiflex C5 cell disruptor (Avestin). Cell debris was removed by ultracentrifugation (45,000 rpm, 30 min, 4 °C), and the resulting cell supernatant was loaded onto a column containing ∼7 ml of Ni-NTA resin, which was pre-equilibrated with lysis buffer. Column flow-through was discarded, and the resin was washed with lysis buffer (40 ml × 2) to remove residual nonspecifically bound proteins. His_6-tagged proteins were eluted from the column with 4 × 12 ml portions of elution buffer (50 mM K_2HPO_4, 500 mM NaCl, 5 mM β-mercaptoethanol, 300 mM imidazole, 10% glycerol, pH 8) and dialyzed for ∼18 h in 1.8 l of dialysis buffer (50 mM K_2HPO_4, 150 mM NaCl, 1 mM DTT, pH 8) using 10,000 MWCO SnakeSkin (ThermoFisher) dialysis tubing. The resulting protein solutions were concentrated by centrifugal filtration

(Amicon Ultra 15 ml, 30,000 MWCO) and flash frozen as ~50 μl beads in liquid nitrogen prior to storage at −80 °C. The concentration of final protein solution was quantified prior to flash freezing by measuring optical absorbance at 280 nm with the predicted molar extinction coefficient (ε = 86,340 M^{-1} cm^{-1}, SgDesD).

In vitro *reconstitution of DesD activity*

Reaction mixtures were prepared in ddi water and contained final working concentrations of 10 mM $MgCl_2$, 25 mM KH_2PO_4, 5.9 mM K_2HPO_4, 10% glycerol (v/v), 0.15 mM of HSC, and 3 mM of ATP. Then, 2.0 to 36.7 μM of DesD ortholog (SgDesD, SvDesD, ScDesD, or SpDesD) were added to initiate the reaction. The reaction mixtures were incubated at RT. Aliquots were taken from each reaction mixture at specified time points and quenched by the addition of an equal volume of MeOH. The quenched samples were then centrifuged, filtered, and analyzed *via* ESI LC-MS in positive ion mode with monitoring of $[M + H]^+$ ions corresponding to the predicted *m/z* values of the expected products *di*-HSC (419), DFOG (619), and DFOE (601).

DesD AMP formation assay

Reaction mixtures contained final working concentrations of 30.9 mM KH_2PO_4, 4 U/ml MK, 8.4 U/ml pyruvate kinase, 12.6 U/ml LDH, 1 mM phosphoenolpyruvate, 10 mM $MgCl_2$, 10% glycerol (v/v), 0.2 mM NADH, and 3 mM ATP and variable concentrations of HSC (0.1–2.0 mM). A 140 μl aliquot of the reaction master mixture was added to a well in a 96-well plate followed by 40 μl of properly diluted HSC stock solution to provide the desired concentration gradient. After equilibrating the plates for 5 min, reactions were initiated by the addition of 20 μl of 2 μM DesD stock solution to provide a final working concentration of 200 nM DesD. The final working volume for each reaction was 200 μl, and the final pH of the working reaction mixture was ~7.2. The reactions were monitored by optical absorbance at 340 nm for the consumption of NADH at RT using SpectraMax Plus 384 Microplate Reader for 60 min. Reactions were performed in duplicate as independent trials. The apparent V_{max} of each DesD ortholog was calculated by fitting the curve of apparent velocity (μM/min) *versus* the logarithm of HSC concentration using nonlinear regression (steady-state saturation kinetics [Michaelis–Menten] or enzyme kinetics with substrate inhibition) in GraphPad Prism v7.0b (GraphPad Software).

Inhibition of DesD by HSC-AMS

To optimize the inhibition of HSC-AMS, 2 μM of ScDesD or SgDesD was preincubated with 150 μM HSC-AMS for 30 min at RT in a reaction mixture consisting of 10 mM $MgCl_2$, 25 mM KH_2PO_4, 5.9 mM K_2HPO_4, and 10% glycerol (v/v). A master mixture of ATP and HSC was added last to initiate the reaction with a final working concentration of 150 μM for each reagent. At each specified time point, an aliquot of the reaction mixture was taken out and mixed with MeOH in 1:1 ratio (v/v) to quench the reaction. The sample was then centrifuged, filtered, and analyzed *via* ESI LC-MS to determine EICs for predicted $[M + H]^+$ ions corresponding to the predicted *m/z* values for products *di*-HSC (419), DFOG (619), and DFOE (601).

Determining IC_{50} of HSC-AMS for ScDesD and SgDesD

Generally, 2 μM of ScDesD or SgDesD was preincubated with 150 μM $NaPP_i$ and varying concentrations of HSC-AMS (150 μM, 100 μM, 75 μM, 50 μM, 25 μM, 12.5 μM, 6.75 μM, and 0 μM) in a reaction mixture consisting of 10 mM $MgCl_2$, 25 mM KH_2PO_4, 5.9 mM K_2HPO_4, and 10% glycerol at RT for 30 min. A master mixture of HSC and ATP was added last to initiate the reaction to afford a final working concentration of 150 μM for both reagents. After 35 min, 100 μl of the reaction mixture was quenched with 500 μl of MeOH, centrifuged, filtered, and analyzed *via* ESI LC-MS. Total DFO production was determined relative to a control reaction void of HSC-AMS (normalized as 100% DFO production) as judged by the combined peak heights corresponding to extracted $[M + H]^+$ ion counts corresponding to predicted *m/z* values for DFOG (619) and DFOE (601) over two independent trials. Peak heights in the EICs were normalized to an internal standard of 10 μM Fmoc-Ala (final concentration). The apparent IC_{50} of HSC-AMS against both ScDesD and SgDesD was calculated by fitting the curve of percent product formation *versus* the logarithm of HSC-AMS concentration using a dose–response (inhibition) function in GraphPad Prism v7.0b.

Purification of DesD proteins for crystallization trials

A single colony of BL21(DE3) cells containing either pET28 expression plasmid was inoculated in 50 ml TB medium containing 50 μg/ml kanamycin and grown overnight at 37 °C. The following day, 8 ml of this starter culture was added to 6 × 0.8 l of TB medium with 50 μg/ml kanamycin and allowed to grow to an absorbance (A_{600}) of 0.6 to 0.8 at 37 °C with shaking at 200 rpm, before being cooled to 4 °C for 30 min. The cultures were then induced with IPTG at 0.5 mM and shaken at 18 °C overnight at 200 rpm for around 20 h. Cells were harvested by centrifugation (4000*g*, 30 min, 4 °C) and stored at −80 °C until purification. Cells were thawed in cold lysis buffer (50 mM HEPES, 400 mM NaCl, 0.25 mM tris(2-carboxyethyl)phosphine (ChemImpex), 10% glycerol, 20 mM imidazole, pH 8.0) prior to sonication on ice (70% amplitude, 10 s on/10 s off, 15 min). The lysate was cleared by ultracentrifugation at 40,000 rpm for 40 min at 4 °C. The supernatant was passed through a 0.45 μm filter and loaded onto 5 ml Ni-NTA cartridge for His-tag affinity purification. Gradient elution was performed over 10 column volumes with lysis buffer supplemented with 250 mM imidazole. Analysis by SDS-PAGE determined adequately pure fractions of DesD protein to be pooled. Combined fractions were concentrated to 50 mg/ml by centrifugation (Amicon Ultra 0.5 Ml 30 kMWCO filtration device, 4000*g*, 10 min, 4 °C) for loading onto a GF 200 Superdex 16/600 column. Gel filtration was performed with buffer (25 mM HEPES, 150 mM NaCl, 0.25 mM tris(2-carboxyethyl)phosphine, pH 7.5) and a single

peak representing DesD protein was concentrated up to 60 mg/ml and flash frozen in liquid nitrogen.

Crystallization of DesD proteins

Initial screening for crystallization was performed with several in-house or commercial sparse matrix screens in a 96-well sitting drop plates using ArtRobbins Gryphon crystallization robot. Crystallization screening of SgDesD was performed at different protein concentrations from 25 to 50 mg/ml, identifying multiple crystallization hits. Further optimization of crystallization was done in hanging-drop plates. A subsequent crystallization hit was further observed at 14 °C with 50 mM Bis–Tris Propane, 200 mM ammonium sulfate, 16% PEG 4000, with protein concentration at 25 to 30 mg/ml produced crystals that routinely diffracted to 2.9 Å. This condition was used for further optimization and cocrystallization with ligands. Protein at 27 to 30 mg/ml was preincubated with 2.5 mM ligands with for 1 h, followed by crystallization in the same crystallization cocktail in 24-well hanging-drop plates at 14 °C. We note that the crystal conditions that led to the structure containing AMP and PP_i also contained 2.5 mM HSC and *N*-hydroxy-*N*-succinylaminopentanol (60), although neither was visible in the electron density. Single large crystals were obtained after 5 to 10 days. To obtain quality crystals bound to the inhibitor, unliganded crystals were used as a seed stock to initiate nucleation in protein drops combined with 2.5 mM HSC-AMS inhibitor in the same crystallization cocktail.

An initial hit for SvDesD protein was obtained with an in-house screen and optimized by hanging drop under oil. Final crystals were obtained by sitting drop under oil with SvDesD at 15 mg/ml and a crystallization cocktail of 100 mM potassium citrate, 50 mM MES pH 6.5, and 25% PEG 8000 at 14 °C. Cocrystallization of SvDesD with ATP or ligands was unsuccessful and soaking with ATP caused cracking or loosening of the crystals resulting in poor diffraction.

X-ray data collection and structure determination

Unliganded SgDesD protein crystals were cryoprotected by serial transfer into crystallization cocktail containing 8%, 16%, 24%, and 32% glycerol, followed by flash-freezing into liquid nitrogen. Ligand-bound cocrystals were similarly cryoprotected in 32% glycerol or 24% (±)2-methyl-2,4-pentanediol (Hampton Research) with ligand in the artificial mother liquor. Similarly, unliganded SvDesD crystals were cryoprotected with 8%, 16%, 24%, and 40% glycerol or ethylene and NDSB-201 mixture (60% ethylene glycol and 200 mg/ml NDSB-201). Data collection from single crystals was performed remotely at APS 23 ID-D and SSRL 12-2 beamline. Diffraction data were processed at the beamline server using XDS. Unliganded SgDesD crystal diffracted up to a resolution of 2.7 Å in the space group $C222_1$. Solved before the deposition of the structure of the model of ScDesD (6P63) from *S. coelicolor* (7), which shares 84% sequence identity with SgDesD, the structure of SgDesD was solved by molecular replacement using the NIS portion of DfoC (5O7O, 54% sequence identity) (25) as a search model in PHASER (61). A good solution was obtained with five protein chains in asymmetric unit. Further model building was done in COOT (62) and followed by refinement using PHENIX http://phenix-online.org (63). Unliganded SvDesD crystals diffracted up to 2.3 Å in space group $P4_32_12$. Structure solution was successful using SgDesD as search model with four protein chains per asymmetric unit. Cocrystal structures with ligands were solved using protein atoms from the unliganded SgDesD structure as the search model for molecular replacement with PHASER (61). The final diffraction and refinement statistics are presented in Table S11. All structures and structure factors are deposited with the PDB. The structures of SgDesD are available with the following accession codes: unliganded (7TGJ), Mg·ATP-bound (7TGK), Mg·AMP- and PP_i-bound (7TGL), and HSC-AMS-bound (7TGM). The SvDesD unliganded structure is deposited with accession code (7TGN). Solvent molecules such as glycerol and sulfate ions were added where supported by electron density. Some ions showed modest negative electron density, suggesting they were not present at 100% occupancy. Refinement as a water, however, was insufficient to account for the density.

Molecular docking of ligands into DesD

Molecular docking was done with AutoDock Vina (64) implemented within UCSF Chimera suite (65). The SgDesD protein atoms for chain C were used as the protein. An AMS analog of the trimeric intermediate DFOG (DFOG-AMS) was manually built by extending the HSC-AMS inhibitor with two HSC moieties connected through amide linkages. The DOCK PREP module was used to remove solvent molecules, add incomplete side chains (66), add hydrogen atoms, and add charges. Charges to nonstandard residues were added with ANTECHAMBER, http://ambermd.org/antechamber (67). A search volume of 27 × 29 × 34 Å was created that covered the entire cavity of the SgDesD protein. Default docking parameters were used, with 10 binding modes, an exhaustiveness search value of 8, and a maximal energy difference of 3 kcal/mol.

Data availability

The structures of SgDesD are available with the following accession codes in the Protein Data Bank: unliganded (7TGJ), Mg·ATP-bound (7TGK), Mg·AMP- and PP_i-bound (7TGL), HSC-AMS-bound (7TGM). The SvDesD unliganded structure is deposited with accession code (7TGN). Nucleotide sequences from whole genome DNA sequencing of *Streptomyces violaceus* DSM 8286 (SvDesD) and *Streptomyces griseoflavus* DSM 40698 (SgDesD) are available *via* GenBank under accession numbers OM145979 and OM145980, respectively.

Supporting information—Supplementary figures, supplementary tables, compound characterization data (NMR), and compound purity analysis (LC-MS) are provided in the supporting information document. This article contains supporting information (43, 47, 68–71).

Funding and additional information—Research was supported by NSF CAREER Award 1654611 to T.A.W., and NIH Award R35GM136235 to A.M.G. GM/CA@APS has been funded by the National Cancer Institute (ACB-12002) and the National Institute of General Medical Sciences (AGM-12006, P30GM138396). This research used resources of the Advanced Photon Source, a U.S. Department of Energy (DOE) Office of Science User Facility operated for the DOE Office of Science by Argonne National Laboratory under Contract No. DE-AC02-06CH11357. The Eiger 16M detector at GM/CA-XSD was funded by NIH grant S10 OD012289. Use of the Stanford Synchrotron Radiation Lightsource, SLAC National Accelerator Laboratory, is supported by the U.S. Department of Energy, Office of Science, Office of Basic Energy Sciences under Contract No. DE-AC02-76SF00515. The SSRL Structural Molecular Biology Program is supported by the DOE Office of Biological and Environmental Research, and by the National Institutes of Health, National Institute of General Medical Sciences (P30GM133894).

Abbreviations—The abbreviations used are: AMS, ((*2R*,*3S*,*4R*,*5R*)-5-(6-amino-9H-purin-9-yl)-3,4-dihydroxytetrahydrofuran-2-yl) methyl sulfamate; DFO, desferrioxamine; DMF, *N*,*N*-dimethylformamide; EIC, extracted ion chromatogram; ESI, electrospray ionization; HAC, N^1-hydroxy-N^1-acetyl-cadaverine; HSC, N^1-hydroxy-N^1-succinyl-cadaverine; LDH, lactate dehydrogenase; MK, myokinase; NHS, *N*-hydroxysuccinimide; Ni-NTA, nickel-nitrilotriacetate; NIS, nonribosomal-peptide-synthetase-independent siderophore; NRPS, nonribosomal peptide synthetase; PDB, Protein Data Bank; TB, terrific broth; THF, tetrahydrofuran; TrocNHOBn, 2,2,2-trichloroethyl (benzyloxy)carbamate.

References

1. Cruz-Morales, P., Ramos-Aboites, H. E., Licona-Cassani, C., Selem-Mójica, N., Mejía-Ponce, P. M., Souza-Saldívar, V., *et al.* (2017) Actinobacteria phylogenomics, selective isolation from an iron oligotrophic environment and siderophore functional characterization, unveil new desferrioxamine traits. *FEMS Microbiol. Ecol.* **93**, fix086
2. Hider, R. C., and Kong, X. (2010) Chemistry and biology of siderophores. *Nat. Prod. Rep.* **27**, 637–657
3. Al Shaer, D., Al Musaimi, O., de la Torre, B. G., and Albericio, F. (2020) Hydroxamate siderophores: natural occurrence, chemical synthesis, iron binding affinity and use as Trojan horses against pathogens. *Eur. J. Med. Chem.* **208**, 112791
4. Barona-Gómez, F., Wong, U., Giannakopulos, A. E., Derrick, P. J., and Challis, G. L. (2004) Identification of a cluster of genes that directs desferrioxamine biosynthesis in Streptomyces coelicolor M145. *J. Am. Chem. Soc.* **126**, 16282–16283
5. Ronan, J. L., Kadi, N., McMahon, S. A., Naismith, J. H., Alkhalaf, L. M., and Challis, G. L. (2018) Desferrioxamine biosynthesis: diverse hydroxamate assembly by substrate-tolerant acyl transferase DesC. *Philos. Trans. R. Soc. Lond. B. Biol. Sci.* **373**, 20170068
6. Dell, M., Dunbar, K. L., and Hertweck, C. (2021) Ribosome-independent peptide biosynthesis: the challenge of a unifying nomenclature. *Nat. Prod. Rep.* **39**, 453–459
7. Hoffmann, K. M., Goncuian, E. S., Karimi, K. L., Amendola, C. R., Mojab, Y., Wood, K. M., *et al.* (2020) Cofactor complexes of DesD, a model enzyme in the virulence-related NIS synthetase family. *Biochemistry* **59**, 3427–3437
8. Kadi, N., Oves-Costales, D., Barona-Gomez, F., and Challis, G. L. (2007) A new family of ATP-dependent oligomerization-macrocyclization biocatalysts. *Nat. Chem. Biol.* **3**, 652–656
9. Senges, C. H. R., Al-Dilaimi, A., Marchbank, D. H., Wibberg, D., Winkler, A., Haltli, B., *et al.* (2018) The secreted metabolome of Streptomyces chartreusis and implications for bacterial chemistry. *Proc. Natl. Acad. Sci. U. S. A.* **115**, 2490–2495
10. Bickel, H., Mertens, P., Prelog, V., Seibl, J., and Walser, A. (1965) Constitution of ferrimycin A1. Antimicrob. *Agents Chemother.* **5**, 951–957
11. Bickel, H., Mertens, P., Prelog, V., Seibl, J., and Walser, A. (1966) Stoffwechselprodukte von mikroorganismen—53: ueber die konstitution von ferrimycin A1. *Tetrahedron* **22**, 171–179
12. Vértesy, L., Aretz, W., Fehlhaber, H.-W., and Kogler, H. (1995) Salmycin A–D, Antibiotika aus Streptomyces violaceus, DSM 8286, mit Siderophor-Aminoglycosid-Struktur. *Helv. Chim. Acta* **78**, 46–60
13. Challis, G. L. (2005) A widely distributed bacterial pathway for siderophore biosynthesis independent of nonribosomal peptide synthetases. *Chembiochem* **6**, 601–611
14. Carroll, C. S., and Moore, M. M. (2018) Ironing out siderophore biosynthesis: a review of non-ribosomal peptide synthetase (NRPS)-independent siderophore synthetases. *Crit. Rev. Biochem. Mol. Biol.* **53**, 356–381
15. Oves-Costales, D., Kadi, N., and Challis, G. L. (2009) The long-overlooked enzymology of a nonribosomal peptide synthetase-independent pathway for virulence-conferring siderophore biosynthesis. *Chem. Commun. (Camb)*, 6530–6541. https://doi.org/10.1039/B913092F
16. Gulick, A. M. (2009) Conformational dynamics in the Acyl-CoA synthetases, adenylation domains of non-ribosomal peptide synthetases, and firefly luciferase. *ACS Chem. Biol.* **4**, 811–827
17. Schmelz, S., and Naismith, J. H. (2009) Adenylate-forming enzymes. *Curr. Opin. Struct. Biol.* **19**, 666–671
18. Mydy, L. S., Bailey, D. C., Patel, K. D., Rice, M. R., and Gulick, A. M. (2020) The siderophore synthetase IucA of the aerobactin biosynthetic pathway uses an ordered mechanism. *Biochemistry* **59**, 2143–2153
19. Schmelz, S., Kadi, N., McMahon, S. A., Song, L., Oves-Costales, D., Oke, M., *et al.* (2009) AcsD catalyzes enantioselective citrate desymmetrization in siderophore biosynthesis. *Nat. Chem. Biol.* **5**, 174–182
20. Bailey, D. C., Drake, E. J., Grant, T. D., and Gulick, A. M. (2016) Structural and functional characterization of aerobactin synthetase IucA from a hypervirulent pathotype of Klebsiella pneumoniae. *Biochemistry* **55**, 3559–3570
21. Tang, J., Ju, Y., Zhou, J., Guo, J., Gu, Q., Xu, J., *et al.* (2020) Structural and biochemical characterization of SbnC as a representative type B siderophore synthetase. *ACS Chem. Biol.* **15**, 2731–2740
22. Oke, M., Carter, L. G., Johnson, K. A., Liu, H., McMahon, S. A., Yan, X., *et al.* (2010) The scottish structural proteomics facility: targets, methods and outputs. *J. Struct. Funct. Genomics* **11**, 167–180
23. Nusca, T. D., Kim, Y., Maltseva, N., Lee, J. Y., Eschenfeldt, W., Stols, L., *et al.* (2012) Functional and structural analysis of the siderophore synthetase AsbB through reconstitution of the petrobactin biosynthetic pathway from Bacillus anthracis. *J. Biol. Chem.* **287**, 16058–16072
24. Bailey, D. C., Alexander, E., Rice, M. R., Drake, E. J., Mydy, L. S., Aldrich, C. C., *et al.* (2018) Structural and functional delineation of aerobactin biosynthesis in hypervirulent Klebsiella pneumoniae. *J. Biol. Chem.* **293**, 7841–7852
25. Salomone-Stagni, M., Bartho, J. D., Polsinelli, I., Bellini, D., Walsh, M. A., Demitri, N., *et al.* (2018) A complete structural characterization of the desferrioxamine E biosynthetic pathway from the fire blight pathogen Erwinia amylovora. *J. Struct. Biol.* **202**, 236–249
26. Schmelz, S., Botting, C. H., Song, L., Kadi, N. F., Challis, G. L., and Naismith, J. H. (2011) Structural basis for acyl acceptor specificity in the achromobactin biosynthetic enzyme AcsD. *J. Mol. Biol.* **412**, 495–504
27. Nolan, K. P., Font, J., Sresutharsan, A., Gotsbacher, M. P., Brown, C. J. M., Ryan, R. M., *et al.* (2022) Acetyl-CoA-mediated post-biosynthetic modification of desferrioxamine B generates N- and N-O-acetylated isomers controlled by a pH switch. *ACS Chem. Biol.* **17**, 426–437
28. Rütschlin, S., and Böttcher, T. (2018) Dissecting the mechanism of oligomerization and macrocyclization reactions of NRPS-independent siderophore synthetases. *Chemistry* **24**, 16044–16051

29. Rütschlin, S., Gunesch, S., and Böttcher, T. (2017) One enzyme, three metabolites: shewanella algae controls siderophore production *via* the cellular substrate pool. *Cell Chem. Biol.* **24**, 598–604.e10
30. Rütschlin, S., Gunesch, S., and Böttcher, T. (2018) One enzyme to build them all: ring-size engineered siderophores inhibit the swarming motility of Vibrio. *ACS Chem. Biol.* **13**, 1153–1158
31. Ferreras, J. A., Ryu, J. S., Di Lello, F., Tan, D. S., and Quadri, L. E. N. (2005) Small-molecule inhibition of siderophore biosynthesis in Mycobacterium tuberculosis and Yersinia pestis. *Nat. Chem. Biol.* **1**, 29–32
32. Finking, R., Neumüller, A., Solsbacher, J., Konz, D., Kretzschmar, G., Schweitzer, M., *et al.* (2003) Aminoacyl adenylate substrate analogues for the inhibition of adenylation domains of nonribosomal peptide synthetases. *Chembiochem* **4**, 903–906
33. Qiao, C., Wilson, D. J., Bennett, E. M., and Aldrich, C. C. (2007) A mechanism-based aryl carrier protein/thiolation domain affinity probe. *J. Am. Chem. Soc.* **129**, 6350–6351
34. Sikora, A. L., Wilson, D. J., Aldrich, C. C., and Blanchard, J. S. (2010) Kinetic and inhibition studies of dihydroxybenzoate-AMP ligase from Escherichia coli. *Biochemistry* **49**, 3648–3657
35. Gadakh, B., Smaers, S., Rozenski, J., Froeyen, M., and Van Aerschot, A. (2015) 5'-(N-aminoacyl)-sulfonamido-5'-deoxyadenosine: attempts for a stable alternative for aminoacyl-sulfamoyl adenosines as aaRS inhibitors. *Eur. J. Med. Chem.* **93**, 227–236
36. Rath, V. L., Silvian, L. F., Beijer, B., Sproat, B. S., and Steitz, T. A. (1998) How glutaminyl-tRNA synthetase selects glutamine. *Structure* **6**, 439–449
37. Ueda, H., Shoku, Y., Hayashi, N., Mitsunaga, J., ichi, In, Y., Doi, M., *et al.* (1991) X-ray crystallographic conformational study of 5'-O-[N-(L-alanyl)-sulfamoyl]adenosine, a substrate analogue for alanyl-tRNA synthetase. *Biochim. Biophys. Acta* **1080**, 126–134
38. Ciulli, A., Scott, D. E., Ando, M., Reyes, F., Saldanha, S. A., Tuck, K. L., *et al.* (2008) Inhibition of Mycobacterium tuberculosis pantothenate synthetase by analogues of the reaction intermediate. *Chembiochem* **9**, 2606–2611
39. Duckworth, B. P., Geders, T. W., Tiwari, D., Boshoff, H. I., Sibbald, P. A., Barry, C. E., *et al.* (2011) Bisubstrate adenylation inhibitors of biotin protein ligase from Mycobacterium tuberculosis. *Chem. Biol.* **18**, 1432–1441
40. Kuhn, M. L., Alexander, E., Minasov, G., Page, H. J., Warwrzak, Z., Shuvalova, L., *et al.* (2016) Structure of the essential Mtb FadD32 enzyme: a promising drug target for treating tuberculosis. *ACS Infect. Dis.* **2**, 579–591
41. Kadi, N., Song, L., and Challis, G. L. (2008) Bisucaberin biosynthesis: an adenylating domain of the BibC multi-enzyme catalyzes cyclodimerization of N-hydroxy-N-succinylcadaverine. *Chem. Commun. (Camb).*, 5119–5121. https://doi.org/10.1039/B813029A
42. Kadi, N., Arbache, S., Song, L., Oves-Costales, D., and Challis, G. L. (2008) Identification of a gene cluster that directs putrebactin biosynthesis in shewanella species: PubC catalyzes cyclodimerization of N-hydroxy-N-succinylputrescine. *J. Am. Chem. Soc.* **130**, 10458–10459
43. Gunter, K., Toupet, C., and Schupp, T. (1993) Characterization of an iron-regulated promoter involved in desferrioxamine B synthesis in Streptomyces pilosus: repressor-binding site and homology to the diphtheria toxin gene promoter. *J. Bacteriol.* **175**, 3295–3302
44. Codd, R., Richardson-Sanchez, T., Telfer, T. J., and Gotsbacher, M. P. (2018) Advances in the chemical biology of desferrioxamine B. *ACS Chem. Biol.* **13**, 11–25
45. Blin, K., Shaw, S., Kloosterman, A. M., Charlop-Powers, Z., Van Wezel, G. P., Medema, M. H., *et al.* (2021) antiSMASH 6.0: improving cluster detection and comparison capabilities. *Nucl. Acids Res.* **49**, W29–W35
46. Ghosh, M., and Miller, M. J. (1996) Synthesis and *in vitro* antibacterial activity of spermidine-based mixed catechol- and hydroxamate-containing siderophore–vancomycin conjugates. *Bioorg. Med. Chem.* **4**, 43–48
47. Kopp, L. E., and Miech, R. P. (1972) Nonlinear enzymatic cycling systems: the exponential cycling system: i. Mathematical models. *J. Biol. Chem.* **247**, 3558–3563
48. Qiao, C., Gupte, A., Boshoff, H. I., Wilson, D. J., Bennett, E. M., Somu, R. V., *et al.* (2007) 5'-O-[(N-acyl)sulfamoyl]adenosines as antitubercular agents that inhibit MbtA: an adenylation enzyme required for siderophore biosynthesis of the mycobactins. *J. Med. Chem.* **50**, 6080–6094
49. Somu, R. V., Boshoff, H., Qiao, C., Bennett, E. M., Barry, C. E., and Aldrich, C. C. (2006) Rationally designed nucleoside antibiotics that inhibit siderophore biosynthesis of Mycobacterium tuberculosis. *J. Med. Chem.* **49**, 31–34
50. Fan, F., Luxenburger, A., Painter, G. F., and Blanchard, J. S. (2007) Steady-state and pre-steady-state kinetic analysis of Mycobacterium smegmatis cysteine ligase (MshC). *Biochemistry* **46**, 11421–11429
51. Kamtekar, S., Kennedy, W. D., Wang, J., Stathopoulos, C., Söll, D., and Steitz, T. A. (2003) The structural basis of cysteine aminoacylation of tRNAPro by prolyl-tRNA synthetases. *Proc. Natl. Acad. Sci. U. S. A.* **100**, 1673–1678
52. Koizumi, M., Hiratake, J., Nakatsu, T., Kato, H., and Oda, J. N. I. (1999) A potent transition-state analogue inhibitor of Escherichia coli asparagine synthetase A. *J. Am. Chem. Soc.* **121**, 5799–5800
53. Lux, M. C., Standke, L. C., and Tan, D. S. (2019) Targeting adenylate-forming enzymes with designed sulfonyladenosine inhibitors. *J. Antibiot. (Tokyo)* **72**, 325–349
54. Kadi, N., and Challis, G. L. (2009) Chapter 17 siderophore biosynthesis. A substrate specificity assay for nonribosomal peptide synthetase-independent siderophore synthetases involving trapping of acyl-adenylate intermediates with hydroxylamine. *Methods Enzymol.* **458**, 431–457
55. Linne, U., and Marahiel, M. A. (2004) Reactions catalyzed by mature and recombinant nonribosomal peptide synthetases. *Methods Enzymol.* **388**, 293–315
56. Lemoine, F., Correia, D., Lefort, V., Doppelt-Azeroual, O., Mareuil, F., Cohen-Boulakia, S., *et al.* (2019) NGPhylogeny.fr: new generation phylogenetic services for non-specialists. *Nucl. Acids Res.* **47**, W260–W265
57. Letunic, I., and Bork, P. (2007) Interactive Tree of Life (iTOL): an online tool for phylogenetic tree display and annotation. *Bioinformatics* **23**, 127–128
58. McWilliam, H., Li, W., Uludag, M., Squizzato, S., Park, Y. M., Buso, N., *et al.* (2013) Analysis tool web services from the EMBL-EBI. *Nucl. Acids Res.* **41**, W597–W600. https://doi.org/10.1093/nar/gkt37
59. Robert, X., and Gouet, P. (2014) Deciphering key features in protein structures with the new ENDscript server. *Nucl. Acids Res.* **42**, W320–W324
60. Wencewicz, T. A., Long, T. E., Möllmann, U., and Miller, M. J. (2013) Trihydroxamate siderophore-fluoroquinolone conjugates are selective sideromycin antibiotics that target Staphylococcus aureus. *Bioconjug. Chem.* **24**, 473–486
61. Zwart, P. H., Afonine, P. V., Grosse-Kunstleve, R. W., Hung, L. W., Ioerger, T. R., McCoy, A. J., *et al.* (2008) Automated structure solution with the PHENIX suite. *Met. Mol. Biol.* **426**, 419–435
62. Emsley, P., and Cowtan, K. (2004) Coot: model-building tools for molecular graphics. *Acta Crystallogr. D. Biol. Crystallogr.* **60**, 2126–2132
63. Adams, P. D., Afonine, P. V., Bunkóczi, G., Chen, V. B., Davis, I. W., Echols, N., *et al.* (2010) PHENIX: a comprehensive python-based system for macromolecular structure solution. *Acta Crystallogr. D. Biol. Crystallogr.* **66**, 213–221
64. Trott, O., and Olson, A. J. (2010) AutoDock Vina: improving the speed and accuracy of docking with a new scoring function, efficient optimization, and multithreading. *J. Comput. Chem.* **31**, 455–461
65. Pettersen, E. F., Goddard, T. D., Huang, C. C., Couch, G. S., Greenblatt, D. M., Meng, E. C., *et al.* (2004) UCSF Chimera–a visualization system for exploratory research and analysis. *J. Comput. Chem.* **25**, 1605–1612
66. Shapovalov, M. V., and Dunbrack, R. L. (2011) A smoothed backbone-dependent rotamer library for proteins derived from adaptive kernel density estimates and regressions. *Structure* **19**, 844–858
67. Wang, J., Wang, W., Kollman, P. A., and Case, D. A. (2006) Automatic atom type and bond type perception in molecular mechanical calculations. *J. Mol. Graph. Model.* **25**, 247–260

68. Schmidt, B. M., Davidson, N. M., Hawkins, A. D. K., Bartolo, R., Majewski, I. J., Ekert, P. G., *et al.* (2018) Clinker: visualizing fusion genes detected in RNA-seq data. *GigaScience* **7**, giy079
69. Vertesy, L., Aretz, W., Fehlhaber, H.-W., and Ganguli, B. N. (1995) Salmycins, a process for their preparation and their use as a pharmaceutical. *US* **5475094**
70. Bentley, S. D., Chater, K. F., Cerdeño-Tárraga, A. M., Challis, G. L., Thomson, N. R., James, K. D., *et al.* (2002) Complete genome sequence of the model actinomycete Streptomyces coelicolor A3(2). *Nature* **417**, 141–147
71. Gaeumann, E., Gaeuman, T., Prelog, V., Vischer, E., and Bickel, H. (1974) Purified ferrimycin and process for obtaining same. *US* **3852424**